IEEE Open Journal of
Industry Applications

Received 16 October 2022; revised 28 February 2023; accepted 29 April 2023. Date of publication 12 May 2023;
date of current version 29 May 2023. The review of this article was arranged by Associate Editor S. Odhano.

Digital Object Identifier 10.1109/OJIA.2023.3275645

First-Order-Delay-Controlled Slip-Angular Frequency for the Dynamic Performance of an Indirect-Field-Orientation-Controlled Induction Motor-Driving Inertial Load

MASAKI NAGATAKI [1] (Graduate Student Member, IEEE), KEIICHIRO KONDO[1] (Member, IEEE), OSAMU YAMAZAKI[2], AND KAZUAKI YUKI[2]

[1]School of Advanced Science and Engineering, Department of Electrical Engineering and Bioscience, Waseda University, Tokyo 1698555, Japan
[2]Toshiba Infrastructure Systems and Solutions Corporation, Tokyo 1838511, Japan

CORRESPONDING AUTHOR: MASAKI NAGATAKI (e-mail: mnagataki@ruri.waseda.jp)

This work was supported by Toshiba Infrastructure Systems and Solutions Corporation.

ABSTRACT Sophisticated torque-current control is required in inertial load-drive applications, such as in electric vehicles and electric railway vehicles, over a wide speed range. However, the conventional indirect-field-orientation control (FOC) lacks the current response during the transient response because the conventional feedforward slip-angular-frequency control causes secondary flux fluctuation. Therefore, this article proposes FOC with first-order-delay slip-angular-frequency control, which reduces the secondary flux fluctuation and realizes high-performance torque-current control during transient response. The proposed method was verified through numerical simulation and small-scale model experiments with a 750 W induction motor and an inertial load.

INDEX TERMS Induction motors (IMs), motor drives, variable speed drives.

NOMENCLATURE

IM	Induction motor.
FOC	Field-orientation-control.
DFOC	Direct-field-orientation-control.
IFOC	Indirect-field-orientation-control.
p	Differential operator.
R_1	Primary resistance.
L_1	Primary self-inductance.
R_2	Secondary resistance.
L_2	Secondary self-inductance.
M	Mutual inductance.
σL_1	Primary leakage inductance in FOC.
T_2	Secondary time constant.
T_d	Time constant of FOC.
$I_{1d}^*,\ I_{1q}^*$	d- and q-axis current command.
$I_{1d},\ I_{1q}$	d- and q-axis current.
$\Phi_{2d},\ \Phi_{2q}$	d- and q-axis secondary flux.
$I_{1dF}^*,\ I_{1qF}^*$	First-order-delay-filtered d- and q-axis current command.
$X_{1d},\ X_{1q}$	Integral value of d- and q-axis current deviation.
ω_s^*	Slip-angular-frequency command.
ω_1	Primary angular frequency command.
ω_r	Secondary angular frequency command.

I. INTRODUCTION

Field-orientation control (FOC) for an induction motor (IM) is a technology that realizes independent control of excitation and torque currents and a high torque performance by controlling the phase angle of the secondary flux [1], [2], [3]. Speed control is not employed, but torque (torque-current) control is employed for inertial load-drive applications, such as electric vehicles and electric railway vehicles. High-performance first-order-delay torque-current control is desirable for inertial load-drive applications over a wide speed range. However, an overshoot of the torque current may occur owing to the transient coupling of the secondary flux during the step response of the torque current in the FOC. This article proposes a method to realize sophisticated torque-current control by

reducing the transient fluctuation of the secondary flux and the overshoot of the torque current with a simple controller configuration.

Direct FOC (DFOC) realizes current control by utilizing direct sensing of the air-gap flux [4], [5], [6]. However, DFOC requires sensors for flux measurement or observers/estimators for flux estimation [7], [8], [9], [10]. However, the controller configuration is complex.

In indirect FOC (IFOC), the phase angle of the secondary flux is controlled by an appropriate slip-angular-frequency command based on the motor parameters and current commands; therefore, sensors for flux measurement and estimators for flux estimation are unnecessary [1], [2], [3]. However, transient misalignment cannot be compensated for because the secondary flux is controlled by feedforward control. The slip-angular-frequency command ω_s^* is given by

$$\omega_s^* = \frac{R_2 I_{1q}^*}{L_2 I_{1dF2}^*} \tag{1}$$

$$I_{1dF2}^* = \frac{1}{1+sT_2} I_{1d}^* \tag{2}$$

where R_2, L_2, I_{1q}^*, I_{1dF2}^*, T_2, and I_{1d}^* represent the secondary resistance, secondary self-inductance, the q-axis current command, filtered value of the d-axis current command, secondary time constant, and d-axis current command, respectively. In the torque control system, the slip-angular-frequency command changes steeply according to (1), when the torque-current command is input. The q-axis secondary flux derived from the voltage equations of the IM, represented in a rotating d- and q-axis reference frame with the primary angular frequency, is expressed as follows:

$$\Phi_{2q} = \frac{R_2 M}{L_2} \frac{-\omega_s^* I_{1d} + \left(s + \frac{R_2}{L_2}\right) I_{1q}}{s^2 + 2\frac{R_2}{L_2} s + \frac{R_2^2}{L_2^2} + \omega_s^{*2}} \tag{3}$$

where M, I_{1d}, and I_{1q} represent the mutual inductance, d-axis current, and q-axis current, respectively. When the slip-angular-frequency command changes steeply, the q-axis secondary flux fluctuates transiently, and the coupling of the secondary flux occurs [11], [12]. Various control applications, such as autodisturbance-rejection control [13], morel reference adaptive system [14], sliding-mode control [14], [15], and neural networks [16], [17], [18], have been proposed to improve the current response. These advanced controllers can reduce the current overshoot by its higher disturbance-rejection capacity. However, the controller configuration is complex, and the controller has many adjustment parameters.

A proportional–integral (PI) current controller is easy to implement because of its simple configuration [19], [20], [21]. However, the PI current controller cannot compensate for the coupling of the secondary flux; thus, it lacks a transient current response [22]. A decoupling control improves a current control performance [23]. Decoupling between the d- and q-axis of the primary side of the IM makes the torque-current response better [24], [25], [26], [27]. However, the secondary flux fluctuation occurs; the torque response degrades when the slip-angular-frequency command changes steeply. Previous studies have focused on the primary side of IMs. Thus, the investigations focusing on the secondary flux response during transient response are insufficient.

In this article, a control method with a simple configuration that realizes sophisticated torque-current control over a wide speed range is proposed. In the proposed method, a first-order-delay filter is added to the slip-angular-frequency controller to reduce the transient fluctuation of the q-axis secondary flux and overshoot of the torque current. The proposed first-order-delay slip-angular-frequency control reduces the transient fluctuation of the q-axis secondary flux and realizes sophisticated torque–current control even during transient response. Therefore, the proposed method makes the controller configuration simple because an additional decoupling controller is not required.

The rest of this article is organized as follows. Section II derives the analytical models of the conventional and proposed IFOC systems. Because the magnitude of the IM transfer function changes with the capacity of the IM, an investigation was conducted for both small-capacity and high-capacity motors. The analysis and numerical simulations with a 750 W IM are presented in Section III. The experimental results with a 750 W IM and inertial load are presented in Section IV. The validity of the analytical model is confirmed by simulation and experiments in Sections III and IV. Assuming electric railway vehicle applications, a 150 kW IM model is used for analysis and numerical simulation in Section V. Finally, Section VI concludes this article.

II. ANALYSIS MODEL OF THE CONVENTIONAL AND PROPOSED CONTROL SYSTEMS

A. MODELING OF THE CONVENTIONAL IFOC

Fig. 1 shows the FOC system of IMs, where R_1, L_1, σL_1, Φ_{2d}, ω_r, ω_1, V_{1d}^*, V_{1q}^*, K_p, K_i, and T_d represent the primary resistance, primary self-inductance, primary leakage inductance, secondary angular frequency, primary angular frequency, d-axis secondary flux, d-axis voltage command, q-axis voltage command, proportional gain, integral gain, and time constant of the current control, respectively; R_{1s}, $(\sigma L_1)_s$, L_{2s}, and M_s represent the set values of the motor parameters in the current controller.

The primary angular frequency is expressed as follows:

$$\omega_1 = \omega_r + \omega_s^*. \tag{4}$$

The slip-angular-frequency command is defined again as

$$\omega_s^* = \frac{R_{2s} I_{1q}^*}{L_{2s} I_{1dF2}^*} \tag{5}$$

where R_{2s} represents the set value of the secondary resistance of the current controller. The PI current-controller gains are expressed as follows:

$$K_p = \frac{(\sigma L_1)_s}{T_d} \tag{6}$$

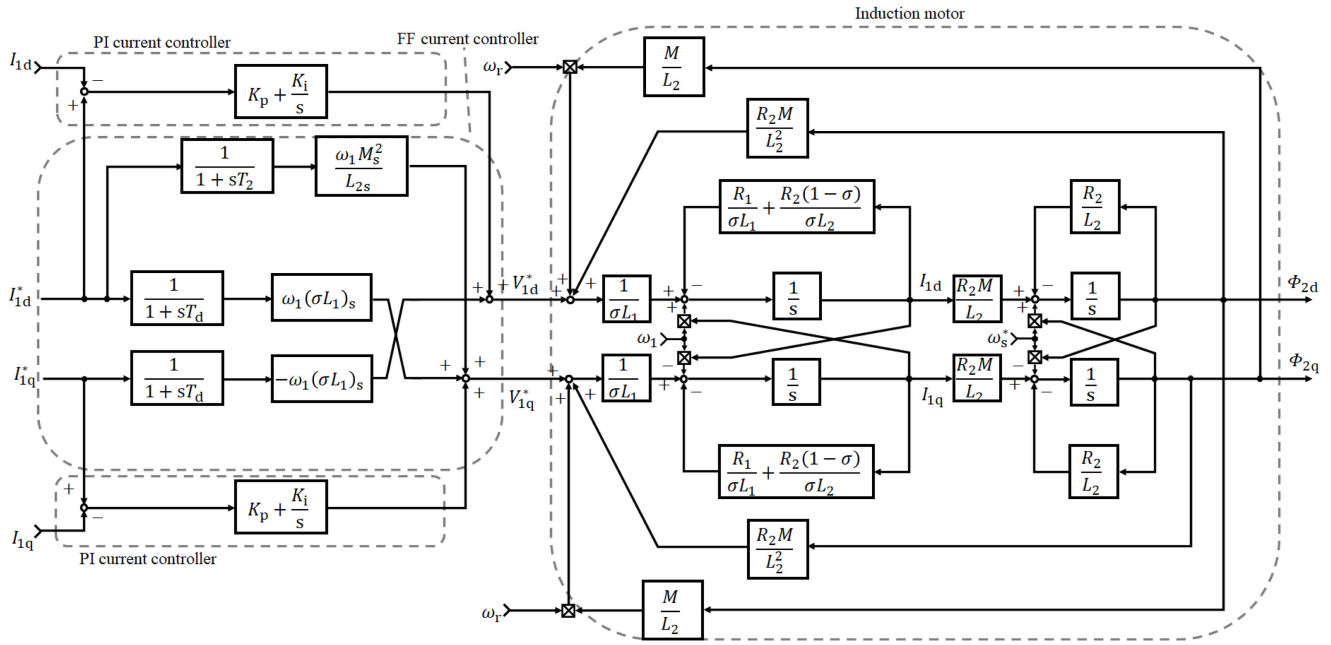

FIGURE 1. Configuration of the IFOC system of IM.

$$K_i = \frac{R_{1s}}{T_d} \tag{7}$$

The voltage equations of the IM represented in a rotating d- and q-axis reference frame with primary angular frequency are expressed as follows:

$$\begin{bmatrix} V_{1d} \\ V_{1q} \\ 0 \\ 0 \end{bmatrix} = \begin{bmatrix} R_1 + p\sigma L_1 & -\omega_1\sigma L_1 & p\left(\frac{M}{L_2}\right) & -\omega_1\left(\frac{M}{L_2}\right) \\ \omega_1\sigma L_1 & R_1 + p\sigma L_1 & \omega_1\left(\frac{M}{L_2}\right) & p\left(\frac{M}{L_2}\right) \\ -R_2\left(\frac{M}{L_2}\right) & 0 & p + \frac{R_2}{L_2} & -\omega_s^* \\ 0 & -R_2\left(\frac{M}{L_2}\right) & \omega_s^* & p + \frac{R_2}{L_2} \end{bmatrix} \times \begin{bmatrix} I_{1d} \\ I_{1q} \\ \Phi_{2d} \\ \Phi_{2q} \end{bmatrix}. \tag{8}$$

The state equations derived from (8) are presented as

$$s\begin{bmatrix} I_{1d} \\ I_{1q} \\ \Phi_{2d} \\ \Phi_{2q} \end{bmatrix} = \begin{bmatrix} -\frac{R_1}{\sigma L_1} - \frac{R_2(1-\sigma)}{\sigma L_2} & \omega_1 & \frac{R_2M}{\sigma L_1 L_2^2} & \omega_r\frac{M}{\sigma L_1 L_2} \\ -\omega_1 & -\frac{R_1}{\sigma L_1} - \frac{R_2(1-\sigma)}{\sigma L_2} & -\omega_r\frac{M}{\sigma L_1 L_2} & \frac{R_2M}{\sigma L_1 L_2^2} \\ R_2\frac{M}{L_2} & 0 & -\frac{R_2}{L_2} & \omega_s^* \\ 0 & R_2\frac{M}{L_2} & -\omega_s^* & -\frac{R_2}{L_2} \end{bmatrix} * \times \begin{bmatrix} I_{1d} \\ I_{1q} \\ \Phi_{2d} \\ \Phi_{2q} \end{bmatrix} + \frac{1}{\sigma L_1}\begin{bmatrix} V_{1d} \\ V_{1q} \\ 0 \\ 0 \end{bmatrix}. \tag{9}$$

The d- and q-axis voltage commands are expressed as

$$V_{1d}^* = K_p\left(I_{1d}^* - I_{1d}\right) + K_i X_{1d} + R_1 I_{1dF}^* - \omega_1\sigma L_1 I_{1qF}^* \tag{10}$$

$$V_{1q}^* = K_p\left(I_{1q}^* - I_{1q}\right) + K_i X_{1q} + R_1 I_{1qF}^* + \omega_1\sigma L_1 I_{1dF}^* + \omega_1\frac{M^2}{L_2} I_{1dF2}^* \tag{11}$$

where the d- and q-axis integrator models are expressed as follows:

$$X_{1d} = \frac{I_{1d}^* - I_{1d}}{s} \tag{12}$$

$$X_{1q} = \frac{I_{1q}^* - I_{1q}}{s}. \tag{13}$$

The d- and q-axis filtered value of current commands are expressed as follows:

$$I_{1dF}^* = \frac{1}{1+sT_d} I_{1d}^* \tag{14}$$

$$I_{1qF}^* = \frac{1}{1+sT_d} I_{1q}^*. \tag{15}$$

The state equations of the IM linearized near the operation point (I_{1d0}, I_{1q0}, Φ_{2d0}, Φ_{2q0}, I_{1dF0}^*, I_{1qF0}^*, I_{1dF20}^*, ω_{10}, ω_{r0}, ω_{s0}^*, I_{1d0}^*, I_{1q0}^*) based on (4)–(9) are presented as follows:

$$s\begin{bmatrix} \delta I_{1d} \\ \delta I_{1q} \\ \delta\Phi_{2d} \\ \delta\Phi_{2q} \\ \delta I_{1dF2}^* \end{bmatrix} = \begin{bmatrix} -\frac{R_1}{\sigma L_1} - \frac{R_2(1-\sigma)}{\sigma L_2} & \omega_{10} & \frac{R_2M}{\sigma L_1 L_2^2} \\ -\omega_{10} & -\frac{R_1}{\sigma L_1} - \frac{R_2(1-\sigma)}{\sigma L_2} & 0 \\ \frac{R_2M}{L_2} & 0 & -\frac{R_2}{L_2} \\ 0 & \frac{R_2M}{L_2} & -\omega_{s0}^* \\ 0 & 0 & -\frac{R_2}{L_2} \end{bmatrix} *$$

$$
\begin{bmatrix}
\frac{R_2M}{\sigma L_1L_2^2} & \frac{\omega_{r0}M}{\sigma L_1L_2} & -\frac{R_{2s}I^*_{1q0}I_{1q0}}{L_{2s}I^*_{1dF20}} \\
-\frac{\omega_{r0}M}{\sigma L_1L_2} & \frac{R_2M}{\sigma L_1L_2^2} & \frac{R_{2s}I^*_{1q0}I_{1d0}}{L_{2s}I^*_{1dF20}} \\
-\frac{R_2}{L_2} & \omega^*_{s0} & -\frac{R_{2s}I^*_{1q0}\Phi_{2q0}}{L_{2s}I^*_{1dF20}} \\
-\omega^*_{s0} & -\frac{R_2}{L_2} & \frac{R_{2s}I^*_{1q0}\Phi_{2d0}}{L_{2s}I^*_{1dF20}} \\
0 & 0 & -\frac{1}{T_2}
\end{bmatrix} *
$$

$$
\times \begin{bmatrix} \delta I_{1d} \\ \delta I_{1q} \\ \delta \Phi_{2d} \\ \delta \Phi_{2q} \\ \delta I^*_{1dF2} \end{bmatrix} + \begin{bmatrix} \frac{1}{\sigma L_1} & 0 \\ 0 & \frac{1}{\sigma L_1} \\ 0 & 0 \\ 0 & 0 \\ 0 & 0 \end{bmatrix} \begin{bmatrix} \delta V_{1d} \\ \delta V_{1q} \end{bmatrix}
$$

$$
+ \begin{bmatrix}
0 & \frac{R_{2s}I_{1q0}}{L_{2s}I^*_{1dF20}} \\
0 & -\frac{R_{2s}I_{1d0}}{L_{2s}I^*_{1dF20}} \\
0 & \frac{R_{2s}\Phi_{2q0}}{L_{2s}I^*_{1dF20}} \\
0 & -\frac{R_{2s}\Phi_{2d0}}{L_{2s}I^*_{1dF20}} \\
\frac{1}{T_2} & 0
\end{bmatrix} \begin{bmatrix} \delta I^*_{1d} \\ \delta I^*_{1q} \end{bmatrix} \tag{16}
$$

where δ represents the infinitesimal displacement and the secondary angular frequency is assumed to be constant. The transfer functions of the current controller based on (2), (4)–(7), and (10)–(15) are expressed as follows:

$$
\begin{bmatrix} \delta V_{1d} \\ \delta V_{1q} \end{bmatrix} = \begin{bmatrix} C_{11}(s) & C_{12}(s) \\ C_{21}(s) & C_{22}(s) \end{bmatrix} \begin{bmatrix} \delta I^*_{1d} \\ \delta I^*_{1q} \end{bmatrix}
$$

$$
+ \begin{bmatrix} -K_p - \frac{K_i}{s} & 0 \\ 0 & -K_p - \frac{K_i}{s} \end{bmatrix} \begin{bmatrix} \delta I_{1d} \\ \delta I_{1q} \end{bmatrix} \tag{17}
$$

$$
C_{11}(s) = K_p + \frac{K_i}{s} + \frac{R_{1s}}{1+sT_d} + \frac{(\sigma L_1)_s R_{2s} I^*_{1qF0} I^*_{1q0}}{L_{2s} I^*_{1dF20}(1+sT_2)} \tag{18}
$$

$$
C_{12}(s) = -(\sigma L_1)_s \left(\frac{\omega_{10}}{1+sT_d} + \frac{R_{2s}I^*_{1qF0}}{L_{2s}I^*_{1dF20}} \right) \tag{19}
$$

$$
C_{21}(s) = \frac{\omega_{10}(\sigma L_1)_s}{1+sT_d}
$$

$$
+ \frac{1}{1+sT_2} \left\{ \frac{\omega_{10}M_s^2}{L_{2s}} - \frac{R_{2s}I^*_{1q0}}{L_{2s}I^*_{1dF20}} \left((\sigma L_1)_s I^*_{1dF0} + \frac{M_s^2 I^*_{1dF20}}{L_{2s}} \right) \right\} \tag{20}
$$

$$
C_{22}(s) = K_p + \frac{K_i}{s} + \frac{R_{1s}}{1+sT_d}
$$

$$
+ \frac{R_{2s}}{L_{2s}I^*_{1dF20}} \left((\sigma L_1)_s I^*_{1dF0} + \frac{M_s^2 I^*_{1dF20}}{L_{2s}} \right). \tag{21}
$$

The state equations of the conventional IFOC system linearized near the operation point (I_{1d0}, I_{1q0}, Φ_{2d0}, Φ_{2q0}, X_{1d0}, X_{1q0}, I^*_{1dF0}, I^*_{1qF0}, I^*_{1dF20}, ω_{10}, ω_{r0}, ω^*_{s0}, I^*_{1d0}, I^*_{1q0}) based on (2) and (4)–(15) are expressed as follows:

$$
\delta \dot{x}_1 = A_1 \delta x_1 + B_1 \delta u_1 \tag{22}
$$

$$
\delta y_1 = C \delta x_1 \tag{23}
$$

$$
\delta x_1 = \begin{bmatrix} \delta I_{1d} & \delta I_{1q} & \delta \Phi_{2d} & \delta \Phi_{2q} & \delta X_{1d} & \delta X_{1q} * \\ * \delta I^*_{1dF} & \delta I^*_{1qF} & \delta I^*_{1dF2} \end{bmatrix}^T \tag{24}
$$

$$
\delta u_1 = \begin{bmatrix} \delta I^*_{1d} \\ \delta I^*_{1q} \end{bmatrix}. \tag{25}
$$

System matrix A_1 and input matrix B_1 are quite complex; therefore, A_1 and B_1 are shown in Appendix A1.

B. PROPOSED SLIP-ANGULAR-FREQUENCY FIRST-ORDER-DELAY CONTROL

The Taylor expansion of (3) with respect to ω^*_s near (I_{1d0}, I_{1q0}, ω^*_{s0}) is expressed as

$$
\Phi_{2q} = -\frac{R_2M}{L_2}
$$

$$
\times \frac{\left(s^2 + \frac{2R_2}{L_2}s + \frac{R_2^2}{L_2^2} - {\omega^*_{s0}}^2 \right) I_{1d0} + 2\omega^*_{s0}\left(s + \frac{R_2}{L_2} \right) I_{1q0}}{\left(s^2 + \frac{2R_2}{L_2}s + \frac{R_2^2}{L_2^2} + {\omega^*_{s0}}^2 \right)^2} \omega^*_s. \tag{26}
$$

Therefore, Φ_{2q} is a second-order-delay system with respect to the input ω^*_s. The undershoot of Φ_{2q} and misalignment of the secondary flux occur when the slip-angular-frequency command changes according to (5). In this study, a method that reduces the high-frequency components of the slip-angular frequency to reduce the fluctuation of Φ_{2q} is proposed.

The proposed first-order-delay-controlled slip-angular-frequency command is presented as

$$
\omega^*_s = \frac{R_{2s}I^*_{1qFs}}{L_{2s}I^*_{1dF2}} \tag{27}
$$

$$
I^*_{1qFs} = \frac{I^*_{1q}}{1+sT_{ds}}. \tag{28}
$$

In the proposed method, a first-order-delay filter is added to the slip-angular-frequency controller to reduce the abrupt change in the slip-angular frequency when the q-axis current command is input. The transient fluctuation of the q-axis secondary flux is reduced and the FOC is realized even during the transient response. Although a high-order-delay filter is assumed, a first-order-delay filter is used to reduce the number of tuning parameters in this study.

C. MODELING OF THE PROPOSED IFOC

The state equations of the IM linearized near the operation point (I_{1d0}, I_{1q0}, Φ_{2d0}, Φ_{2q0}, I^*_{1dF0}, I^*_{1qF0}, I^*_{1dF20}, I^*_{1qFs0}, ω_{10}, ω_{r0}, ω^*_{s0}, I^*_{1d0}, I^*_{1q0}) in the proposed method based on (2), (4),

(9), (27), and (28) are expressed as follows:

$$
s\begin{bmatrix}\delta I_{1d}\\ \delta I_{1q}\\ \delta\Phi_{2d}\\ \delta\Phi_{2q}\\ \delta I^*_{1dF2}\\ \delta I^*_{1qFs}\end{bmatrix}=\begin{bmatrix}-\frac{R_1}{\sigma L_1}-\frac{R_2(1-\sigma)}{\sigma L_2} & \omega_{10}\\ -\omega_{10} & -\frac{R_1}{\sigma L_1}-\frac{R_2(1-\sigma)}{\sigma L_2}\\ \frac{R_2M}{L_2} & 0\\ 0 & \frac{R_2M}{L_2}\\ 0 & 0\\ 0 & 0\end{bmatrix}*
$$

$$
\begin{bmatrix}\frac{R_2M}{\sigma L_1L_2^2} & \frac{\omega_{r0}M}{\sigma L_1L_2} & -\frac{R_{2s}I^*_{1qFs0}I_{1q0}}{L_{2s}I^*_{1dF20}} & \frac{R_{2s}I_{1q0}}{L_{2s}I^*_{1dF20}}\\ -\frac{\omega_{r0}M}{\sigma L_1L_2} & \frac{R_2M}{\sigma L_1L_2^2} & \frac{R_{2s}I^*_{1qFs0}I_{1d0}}{L_{2s}I^*_{1dF20}} & -\frac{R_{2s}I_{1d0}}{L_{2s}I^*_{1dF20}}\\ -\frac{R_2}{L_2} & \omega^*_{s0} & -\frac{R_{2s}I^*_{1qFs0}\Phi_{2q0}}{L_{2s}I^*_{1dF20}} & \frac{R_{2s}\Phi_{2q0}}{L_{2s}I^*_{1dF20}}\\ -\omega^*_{s0} & -\frac{R_2}{L_2} & \frac{R_{2s}I^*_{1qFs0}\Phi_{2d0}}{L_{2s}I^*_{1dF20}} & -\frac{R_{2s}\Phi_{2d0}}{L_{2s}I^*_{1dF20}}\\ 0 & 0 & -\frac{1}{T_2} & 0\\ 0 & 0 & 0 & -\frac{1}{T_{ds}}\end{bmatrix}*
$$

$$
\times\begin{bmatrix}\delta I_{1d}\\ \delta I_{1q}\\ \delta\Phi_{2d}\\ \delta\Phi_{2q}\\ \delta I^*_{1dF2}\\ \delta I^*_{1qFs}\end{bmatrix}+\begin{bmatrix}\frac{1}{\sigma L_1} & 0\\ 0 & \frac{1}{\sigma L_1}\\ 0 & 0\\ 0 & 0\\ 0 & 0\\ 0 & 0\end{bmatrix}\begin{bmatrix}\delta V_{1d}\\ \delta V_{1q}\end{bmatrix}
$$

$$
+\begin{bmatrix}0 & 0\\ 0 & 0\\ 0 & 0\\ 0 & 0\\ \frac{1}{T_2} & 0\\ 0 & \frac{1}{T_{ds}}\end{bmatrix}\begin{bmatrix}\delta I^*_{1d}\\ \delta I^*_{1q}\end{bmatrix}. \tag{29}
$$

The transfer functions of the current controller in the proposed method based on (2), (4), (10)–(15), (27), and (28) are expressed as follows:

$$
\begin{bmatrix}\delta V_{1d}\\ \delta V_{1q}\end{bmatrix}=\begin{bmatrix}C'_{11}(s) & C'_{12}(s)\\ C'_{21}(s) & C'_{22}(s)\end{bmatrix}\begin{bmatrix}\delta I^*_{1d}\\ \delta I^*_{1q}\end{bmatrix}
$$

$$
+\begin{bmatrix}-K_p-\frac{K_i}{s} & 0\\ 0 & -K_p-\frac{K_i}{s}\end{bmatrix}\begin{bmatrix}\delta I_{1d}\\ \delta I_{1q}\end{bmatrix} \tag{30}
$$

$$
C'_{11}(s)=K_p+\frac{K_i}{s}+\frac{R_{1s}}{1+sT_d}+\frac{(\sigma L_1)_sR_{2s}\,I^*_{1qF0}I^*_{1qFs0}}{L_{2s}I^*_{1dF20}(1+sT_2)} \tag{31}
$$

$$
C'_{12}(s)=-(\sigma L_1)_s\left\{\frac{\omega_{10}}{1+sT_d}+\frac{R_{2s}I^*_{1qF0}}{L_{2s}I^*_{1dF20}(1+sT_{ds})}\right\} \tag{32}
$$

$$
C'_{21}(s)=\frac{\omega_{10}(\sigma L_1)_s}{1+sT_d}+\frac{1}{1+sT_2}
$$

$$
\left\{\frac{\omega_{10}M_s^2}{L_{2s}}-\frac{R_{2s}I^*_{1qFs0}}{L_{2s}I^*_{1dF20}}\left((\sigma L_1)_sI^*_{1dF0}+\frac{M_s^2I^*_{1dF20}}{L_{2s}}\right)\right\} \tag{33}
$$

$$
C'_{22}(s)=K_p+\frac{K_i}{s}+\frac{R_{1s}}{1+sT_d}
$$

TABLE 1. Configuration of the IM With Inertia Used for the Experimental Verification

Symbol	Quantity	Value
R_1	Primary resistance	3.8 Ω
L_1	Primary self-inductance	112 mH
R_2	Secondary resistance	2.07 Ω
L_2	Secondary self-inductance	123 mH
M	Mutual inductance	100 mH
σL_1	Primary leakage inductance in FOC	31.4 mH
-	Rated output	750 W
-	Poles	8
-	Rated voltage	200 V
-	Rated frequency	50 Hz
-	Rated current	4.80 A
-	Rated speed	700 r/min
-	Total inertia	0.79 kg · m^2

$$
+\frac{R_{2s}}{L_{2s}I^*_{1dF20}(1+sT_{ds})}\left((\sigma L_1)_sI^*_{1dF0}+\frac{M_s^2I^*_{1dF20}}{L_{2s}}\right). \tag{34}
$$

The state equations of the proposed IFOC system linearized near the operation point (I_{1d0}, I_{1q0}, Φ_{2d0}, Φ_{2q0}, X_{1d0}, X_{1q0}, I^*_{1dF0}, I^*_{1qF0}, I^*_{1dF20}, I^*_{1qFs0}, ω_{10}, ω_{r0}, ω^*_{s0}, I^*_{1d0}, I^*_{1q0}) based on (2), (4), (9)–(15), (27), and (28) are given as follows:

$$
\delta\dot{x}_2=A_2\delta x_2+B_2\delta u_2 \tag{35}
$$

$$
y_2=Cx_2 \tag{36}
$$

$$
\delta x_2=\begin{bmatrix}\delta I_{1d} & \delta I_{1q} & \delta\Phi_{2d} & \delta\Phi_{2q} & \delta X_{1d} & \delta X_{1q} & *\\ & & & & * & \delta I^*_{1dF} & \delta I^*_{1qF} & \delta I^*_{1dF2} & \delta I^*_{1qFs}\end{bmatrix}^T \tag{37}
$$

$$
\delta u_2=\begin{bmatrix}\delta I^*_{1d}\\ \delta I^*_{1q}\end{bmatrix}. \tag{38}
$$

System matrix A_2 and input matrix B_2 are quite complex; therefore, A_2 and B_2 are shown in Appendix A2.

III. ANALYSIS AND VERIFICATION OF THE CONVENTIONAL AND PROPOSED CONTROL SYSTEM WITH A 750 W IM

A. ANALYSIS OF THE CONVENTIONAL AND PROPOSED IFOC

The conventional and proposed IFOC systems were analyzed based on the analytical models derived in Section II. Table 1 summarizes the IFOC of a 750 W IM. Table 2 lists the operational points of the analysis. The target time constant T_d of the IFOC is assumed to be 10 ms in this study. In this section, the time constant T_{ds} of the proposed slip-angular-frequency first-order-delay controller is equivalent to T_d. The determination method for T_{ds} is discussed in Section III-B.

Fig. 2 shows the closed-loop transfer function between δI^*_{1q} and δI_{1q} in the conventional and proposed IFOC systems according to (22)–(25) and (35)–(38) when the primary angular frequency is 250 rad/s. In a conventional IFOC system, the magnitude of the transfer function is relatively large and is a second-order system. Therefore, an overshoot of the q-axis

TABLE 2. Operation Point for the Analysis

Symbol	Quantity	Value
I_{1d0}	d-axis current	4 A
I_{1q0}	q-axis current	5.7 A
Φ_{2d0}	d-axis secondary flux	0.4 Wb
Φ_{2q0}	q-axis secondary flux	0 Wb
X_{1d0}	Integral value of d-axis current deviation	0 A·s
X_{1d0}	Integral value of q-axis current deviation	0 A·s
I^*_{1dF0}	First-order-delay-filtered d-axis current command	4 A
I^*_{1qF0}	First-order-delay-filtered q-axis current command	5.7 A
I^*_{1dF20}	First-order-delay-filtered d-axis current command	4 A
I^*_{1qFs0}	First-order-delay-filtered q-axis current command	5.7 A
I^*_{1d0}	d-axis current command	4 A
I^*_{1q0}	q-axis current command	5.7 A
ω^*_{s0}	Slip-angular-frequency command	24 rad/s
ω_{10}	Primary angular frequency	– rad/s
ω_{r0}	Secondary angular frequency ($\omega_{r0} = \omega_{10} - \omega^*_{s0}$)	– rad/s

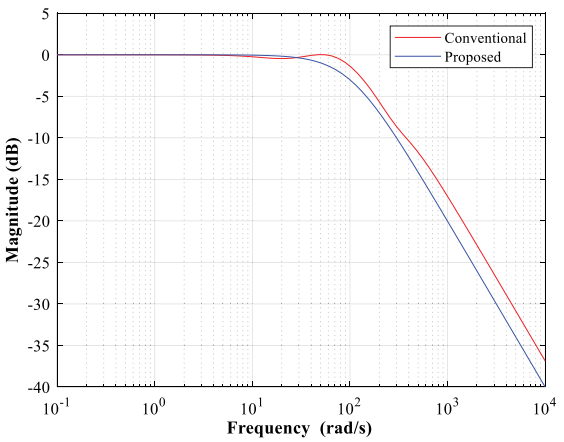

FIGURE 2. Bode plot of the closed-loop transfer function between I^*_{1q} and I_{1q} ($\omega_{10} = 250$ (rad/s)).

current is expected in the step response. In the proposed IFOC system, the magnitude of the transfer function is –3 dB at 100 rad/s, and the maximum value is 0 dB. Therefore, the proposed IFOC system is expected to be a first-order-delay system of 100 rad/s. Fig. 3 shows the closed-loop transfer function between δI^*_{1q} and $\delta\Phi_{2q}$ in the conventional and proposed IFOC systems according to (22)–(25) and (35)–(38), when the primary angular frequency is 250 rad/s. Compared with the conventional IFOC system, the proposed IFOC system reduces the q-axis secondary flux fluctuation because of the first-order-delay slip-angular-frequency control.

Fig. 4 shows the closed-loop transfer function between δI^*_{1q} and δI_{1q} in the conventional and proposed IFOC systems according to (22)–(25) and (35)–(38), when the primary angular

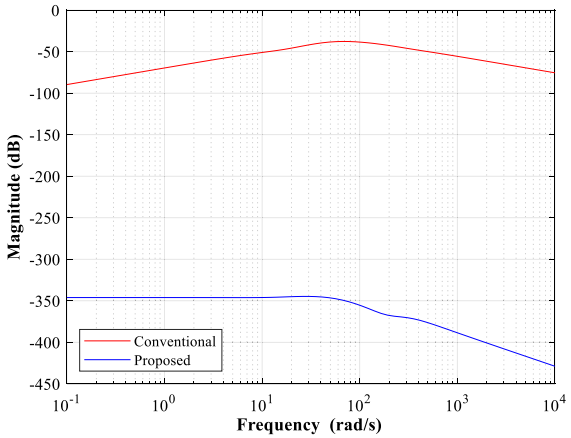

FIGURE 3. Bode plot of the closed-loop transfer function between I^*_{1q} and Φ_{2q} ($\omega_{10} = 250$ (rad/s)).

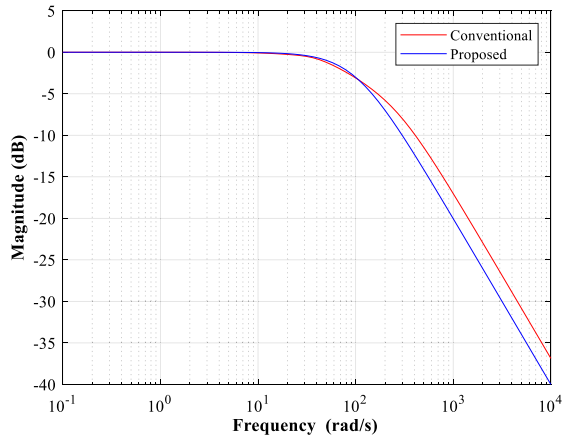

FIGURE 4. Bode plot of the closed-loop transfer function between I^*_{1q} and I_{1q} ($\omega_{10} = 50$ (rad/s)).

frequency is 50 rad/s. In a conventional IFOC system, the magnitude of the transfer function is relatively larger than that of the proposed method, but the peak magnitude is lower than the case of 250 rad/s. In the low-speed region, the response of the conventional IFOC system is expected to be similar to that of the first-order-delay system. Fig. 5 shows the bode plots of the conventional IFOC system. The bode plots of the current controller are based on the transfer function between δI^*_{1q} and δV^*_{1q} according to (16). The bode plots of the IM plant model are based on the transfer function between δV^*_{1q} and δI_{1q} according to (21). The open-loop transfer function between δI^*_{1q} and δI_{1q} is based on (22)–(25). The peak magnitude of the IM plant causes the magnitude of the control system to be high in the high-frequency region when the primary angular frequency is high. Therefore, the magnitude of the closed-loop transfer function of the IFOC system tends to increase near the cutoff frequency when the primary angular frequency is high. This tendency is more noticeable in the case of large-capacity IMs, as shown in Section V, because the inductance of a large-capacity IM is small; and the peak magnitude of the IM plant is larger than that shown in Fig. 5.

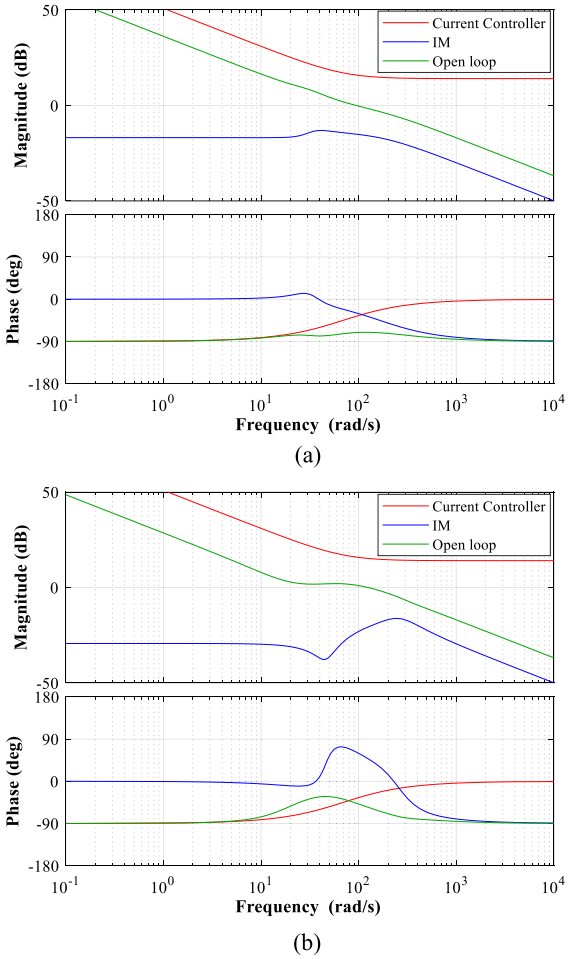

FIGURE 5. Bode plot of the transfer function of the conventional IFOC. (a) $\omega_{10} = 50$ rad/s. (b) $\omega_{10} = 250$ rad/s.

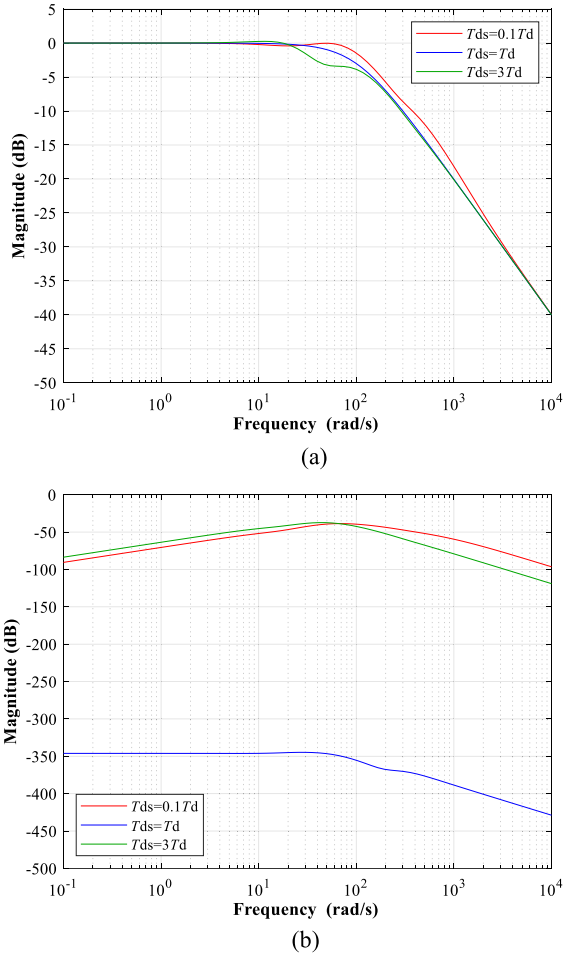

FIGURE 6. Bode plot of the closed-loop transfer function of the proposed IFOC ($T_{ds} = 0.1T_d$, T_d, $3T_d$). (a) $\delta I_{1q}^* \rightarrow \delta I_{1q}$. (b) $\delta I_{1q}^* \rightarrow \delta \Phi_{2q}$.

B. DETERMINATION OF THE TIME CONSTANT T_{ds} IN THE SLIP-ANGULAR-FREQUENCY FIRST-ORDER-DELAY CONTROLLER

Fig. 6 shows the closed-loop transfer function of the proposed IFOC when the primary angular frequency is 250 rad/s and T_{ds} changes.

In the case of a small time constant T_{ds}, the sensitivity of the q-axis secondary flux with respect to the torque-current command increases because the suppression effect of the slip-angular-frequency fluctuation by the first-order-delay filter is reduced. The magnitude of the control system at a frequency of approximately 100 rad/s was large. Therefore, the time constant of the torque-current response is expected to be shorter than the target response time constant T_d, and an overshoot may occur.

In the case of a large time constant T_{ds}, the magnitude of the control system at a frequency of approximately 100 rad/s is small, and the time constant of the torque-current response is expected to be longer than the target response time constant T_d.

When T_{ds} is equal to the time constant T_d of the current controller, the torque-current response is expected to be equal to the target response time constant T_d. The numerator of the transfer function of the q-axis secondary flux based on (3) and (27) is expressed as follows:

$$-\omega_s^* I_{1d} + \left(s + \frac{R_2}{L_2}\right) I_{1q} = -\frac{R_{2s} I_{1qFs}^*}{L_{2s} I_{1dF2}^*} I_{1d} + \left(s + \frac{R_2}{L_2}\right) I_{1q}. \tag{39}$$

The constant term in (39) can be made close to zero by setting the time constant of I_{1qFs}^* to T_d because the torque current I_{1q} is expected to be a response of the time constant T_d. Therefore, the sensitivity of the q-axis secondary flux with respect to the torque-current command can be suppressed by making the time constant of the slip-angular-frequency first-order-delay controller equal to that of the current controller.

C. INFLUENCE OF THE PARAMETER ERROR OF THE SECONDARY RESISTANCE SET VALUE R_{2s}

Assuming a parameter error ΔR_2 with respect to the true secondary resistance value R_2, the secondary resistance set

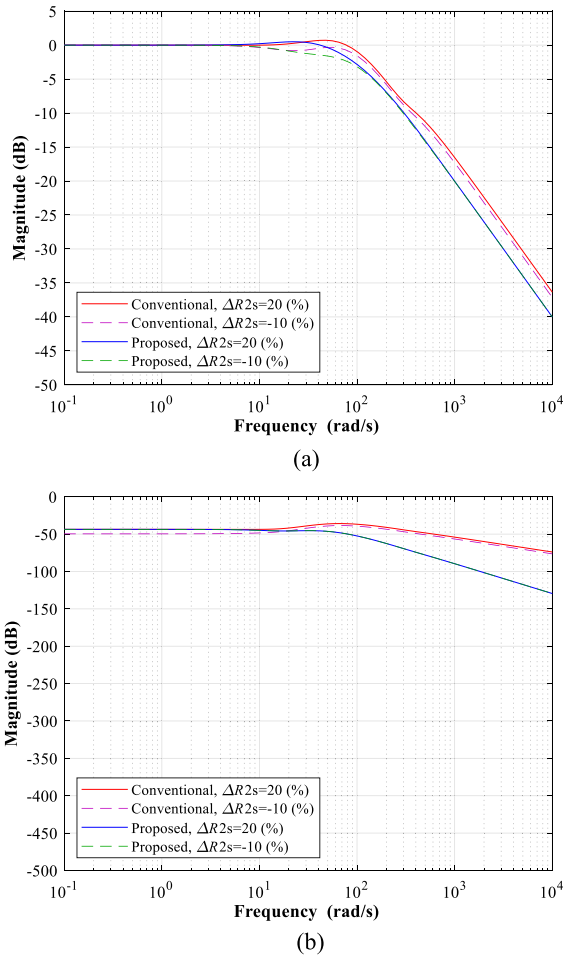

FIGURE 7. Bode plot of the closed-loop transfer function of the conventional and proposed IFOC ($\Delta R_2 = +20,\ -10$ (%)). (a) $\delta I_{1q}^* \rightarrow \delta I_{1q}$. (b) $\delta I_{1q}^* \rightarrow \delta \Phi_{2q}$.

value is defined as follows:

$$R_{2s} = R_2 + \Delta R_2. \tag{40}$$

Fig. 7 shows the closed-loop transfer function of the conventional and proposed IFOC systems when the primary angular frequency is 250 rad/s and ΔR_2 changes. Degradation of the current control performance is inevitable for both the conventional and proposed IFOC systems because the error in the secondary resistance set value causes the misalignment of the secondary flux in a steady state. However, compared with the conventional IFOC, the proposed IFOC makes the magnitude of the control system reduced in a high-frequency region; the secondary flux fluctuation and the torque-current overshoot during transient response are expected to be reduced.

D. NUMERICAL SIMULATION OF THE CONVENTIONAL AND PROPOSED IFOC

A numerical simulation based on Table 2 was conducted to verify the proposed method, including its secondary flux response. In this simulation, pulsewidth-modulation control was not considered because the purpose was to verify the proposed method in principle.

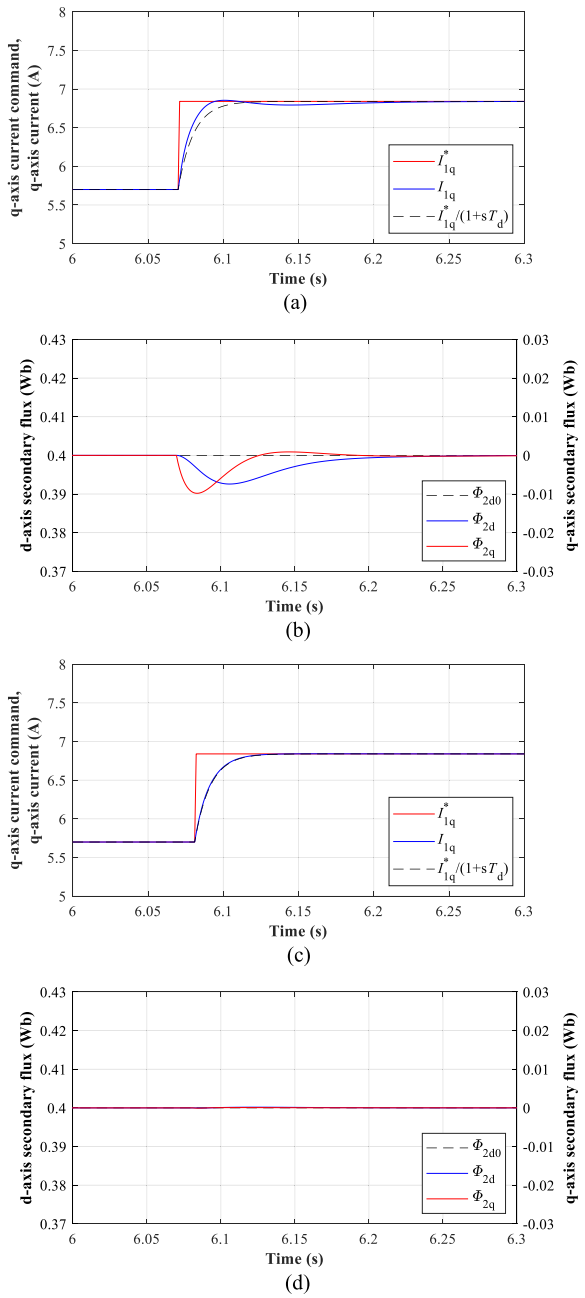

FIGURE 8. Step response in the conventional and proposed IFOC ($\omega_{10} = 250$ rad/s). (a) I_{1q} in the conventional IFOC. (b) Φ_2 in the conventional IFOC. (c) I_{1q} in the proposed IFOC. (d) Φ_2 in the proposed IFOC.

Fig. 8 shows the simulation results of the torque-current step response when the primary angular frequency was 250 rad/s. In the conventional IFOC, the q-axis secondary flux fluctuates transiently when the step q-axis current command is input, and a vibration of the q-axis current occurs owing to the coupling of the secondary flux. In the proposed IFOC, the misalignment is reduced, and the FOC and first-order-delay responses are realized.

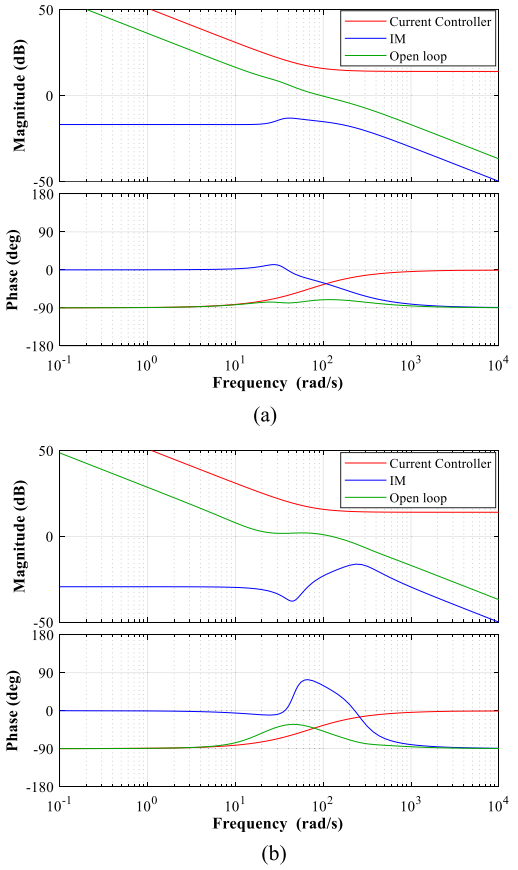

FIGURE 9. Step response in the conventional and proposed IFOC ($\omega_{10} = 50$ rad/s). (a) I_{1q} in the conventional IFOC. (b) Φ_2 in the conventional IFOC. (c) I_{1q} in the proposed IFOC. (d) Φ_2 in the proposed IFOC.

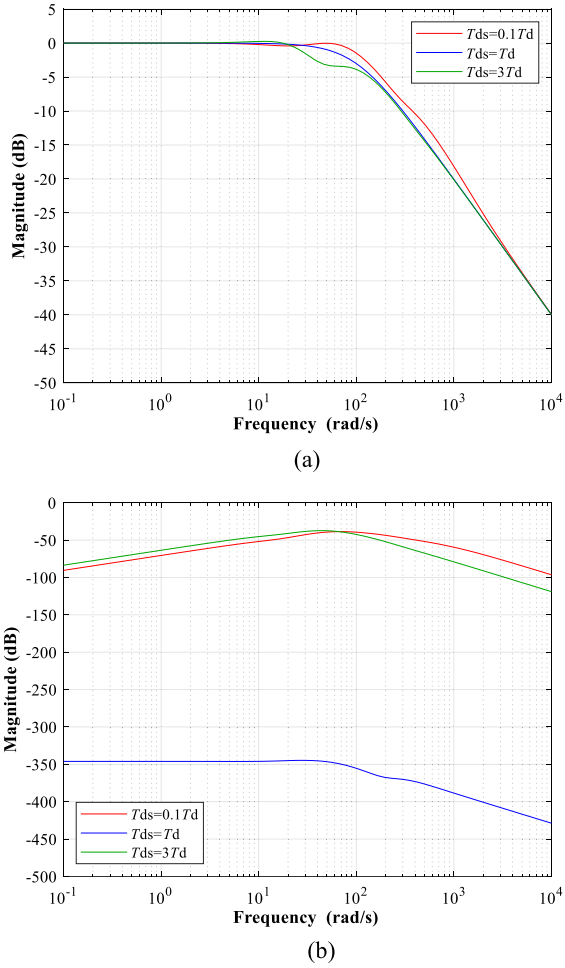

FIGURE 10. Step response in the proposed IFOC ($\omega_{10} = 250$ rad/s, $T_{ds} = 0.1T_d$, $3T_d$). (a) I_{1q} in proposed IFOC ($T_{ds} = 0.1T_d$). (b) Φ_2 in the proposed IFOC ($T_{ds} = 0.1T_d$). (c) I_{1q} in the proposed IFOC ($T_{ds} = 3T_d$). (d) Φ_2 in the proposed IFOC ($T_{ds} = 3T_d$).

Fig. 9 shows the simulation results of the torque-current step response when the primary angular frequency was 50 rad/s. The torque-current response was close to the first-order-delay response of 100 rad/s, even in the conventional IFOC; this result corresponds to the tendency of the analysis in Section III-A.

E. NUMERICAL SIMULATION OF THE PROPOSED IFOC FOR VERIFICATION OF T_{ds}

Fig. 10 shows the simulation results of the torque-current step response when the primary angular frequency was 250 rad/s and T_{ds} is changed. In the case of a small time constant T_{ds}, the torque-current response is faster than the target response, and an overshoot occurs because the magnitude of the control system at a frequency of approximately 100 rad/s is large. In the case of a large time constant T_{ds}, the torque-current response is slower than the target response because the magnitude of the control system at a frequency of approximately 100 rad/s is small. When T_{ds} is not equal to T_d, the suppression effect of the q-axis secondary flux fluctuation degrades, and misalignment of the secondary flux occurs.

F. NUMERICAL SIMULATION OF THE CONVENTIONAL AND PROPOSED IFOC FOR VERIFICATION OF ΔR_2

Figs. 11 and 12 show the simulation results of the torque-current step response when the primary angular frequency was 250 rad/s and ΔR_2 changed. When the set value of the secondary resistance has errors, misalignment of the secondary flux occurs in the steady state; the torque-current control performance is degraded in both the conventional and proposed IFOC systems. However, compared with the conventional IFOC, the proposed IFOC reduces the secondary flux fluctuation and torque-current overshoot during a transient response. The slip-angular-frequency command is calculated based on the secondary resistance in IFOC. Therefore, the misalignment due to ΔR_2 is inevitable. Thus, the correct secondary resistance is needed. However, the proposed control method is very simple construction, and the high torque-current control performance is realized by only tuning the secondary resistance.

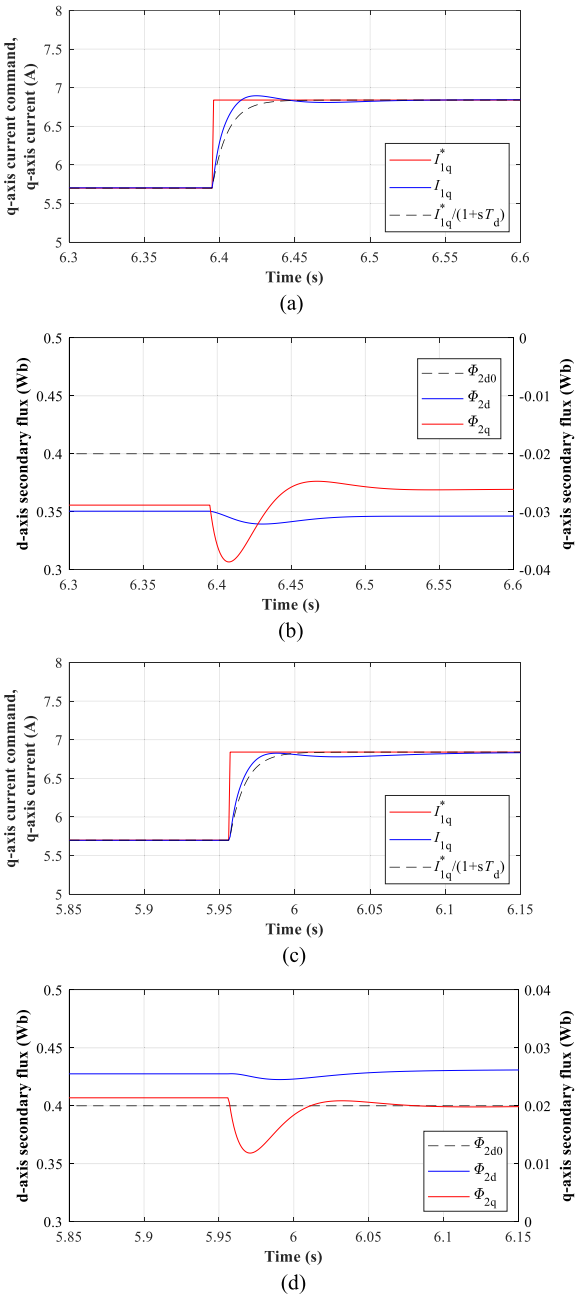

FIGURE 11. Step response in the conventional IFOC ($\omega_{10} = 250$ rad/s, $\Delta R_2 = 20,\ -10$ (%)). (a) I_{1q} in the conventional IFOC ($\Delta R_2 = 20$ (%)). (b) Φ_2 in the conventional IFOC ($\Delta R_2 = 20$ (%)). (c) I_{1q} in the conventional IFOC ($\Delta R_2 = -10$ (%)). (d) Φ_2 in the conventional IFOC ($\Delta R_2 = -10$ (%)).

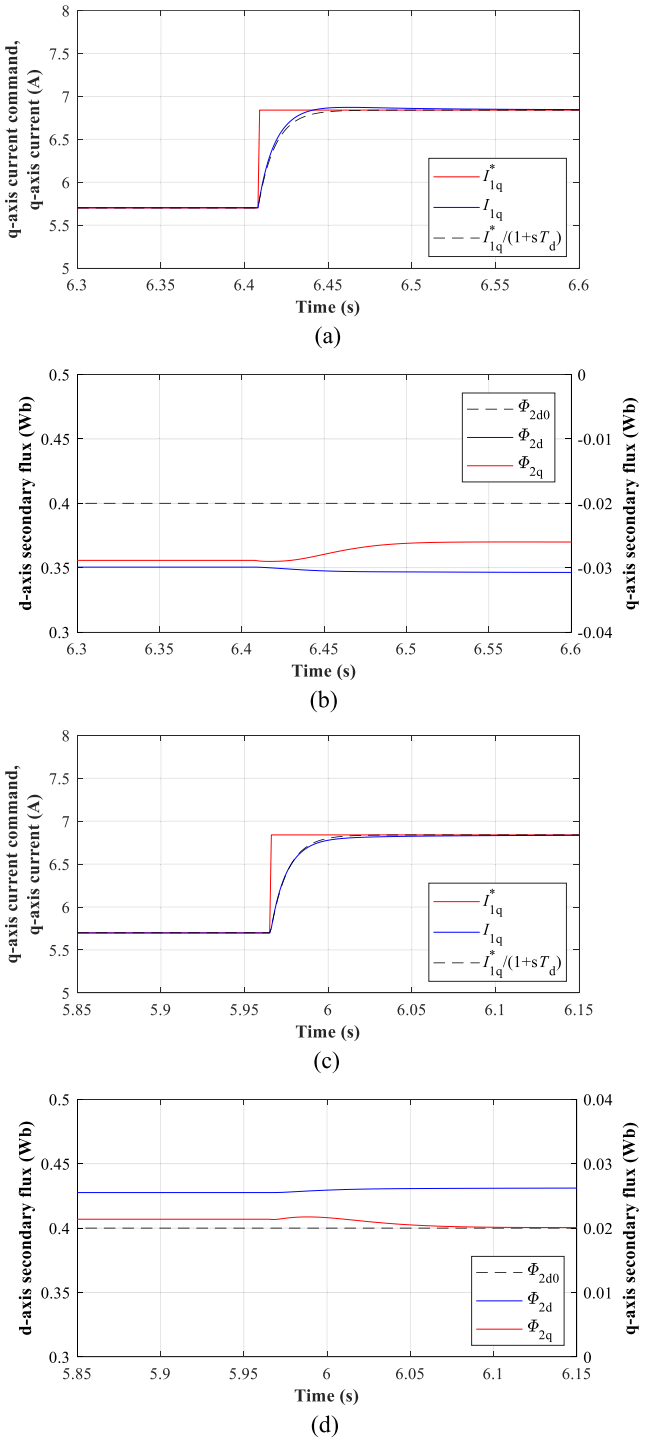

FIGURE 12. Step response in the proposed IFOC ($\omega_{10} = 250$ rad/s, $\Delta R_2 = 20,\ -10$ (%)). (a) I_{1q} in the proposed IFOC ($\Delta R_2 = 20$ (%)). (b) Φ_2 in the proposed IFOC ($\Delta R_2 = 20$ (%)). (c) I_{1q} in the proposed IFOC ($\Delta R_2 = -10$ (%)). (d) Φ_2 in the proposed IFOC ($\Delta R_2 = -10$ (%)).

IV. EXPERIMENTAL VERIFICATION OF THE CONVENTIONAL AND PROPOSED CONTROL SYSTEMS WITH 750 W IM

A. EXPERIMENTS OF THE CONVENTIONAL AND PROPOSED IFOC

Experimental verification was conducted because the dead-time of the inverter, forward voltage of the power semiconductor devices, and harmonic components of the current and voltage were not considered in the numerical simulation. An eight-pole 750 W IM with an inertial load was used for the verification. Table 1 summarizes the IM used for the experimental verification. Fig. 13 shows the configuration of the experimental system. The dc link voltage was 300 V, the sampling frequency was 5 kHz, the d- and q-axis current commands were 4 A and 5.7 A, the time constant of the

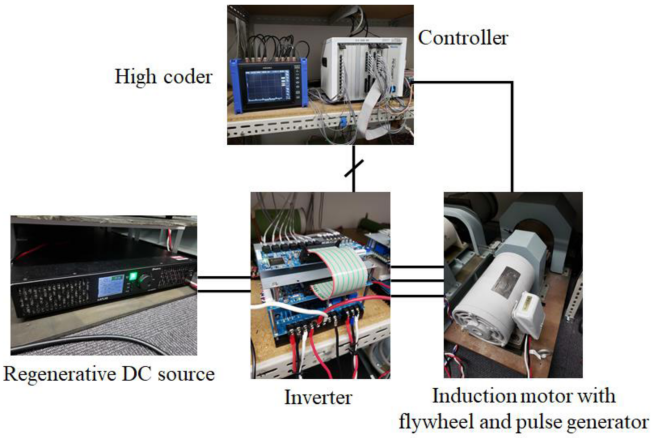

FIGURE 13. Configuration of the experimental system.

current controller T_d was 10 ms, and the time constant of the slip-angular-frequency first-order-delay controller T_{ds} was 10 ms.

Fig. 14 shows the experimental results in acceleration and deceleration operation. Since the proposed first-order-delay slip-angular-frequency control is a method to improve the transient characteristics of the torque current, there is no difference between the conventional and proposed methods in the steady-state operation.

Fig. 15 shows the experimental waveforms of the torque-current step response when the primary angular frequency was 250 rad/s. The proposed IFOC realizes a torque-current response that is closer to the target response than the conventional IFOC.

Fig. 16 shows the experimental waveforms of the torque-current step response when the primary angular frequency is 50 rad/s, wherein the sixth-order harmonic component of the fundamental frequency owing to the deadtime increases the current ripple. The torque-current response is the first-order-delay response of 100 rad/s even in the conventional IFOC; this result corresponds to the tendency of the analysis.

B. EXPERIMENTS OF THE PROPOSED IFOC FOR VERIFICATION OF T_{ds}

Fig. 17 shows the experimental waveforms of the torque-current step response when the primary angular frequency was 250 rad/s and T_{ds} changes. In the case of a small time constant T_{ds}, the torque-current response is faster than the target response, and an overshoot occurs because the magnitude of the control system around the frequency of 100 rad/s is large. In the case of a large time constant T_{ds}, the torque-current response is slower than the target response because the magnitude of the control system at a frequency of approximately 100 rad/s is small. Therefore, the time constant of the slip-angular-frequency first-order-delay controller was determined to be equal to that of the current controller.

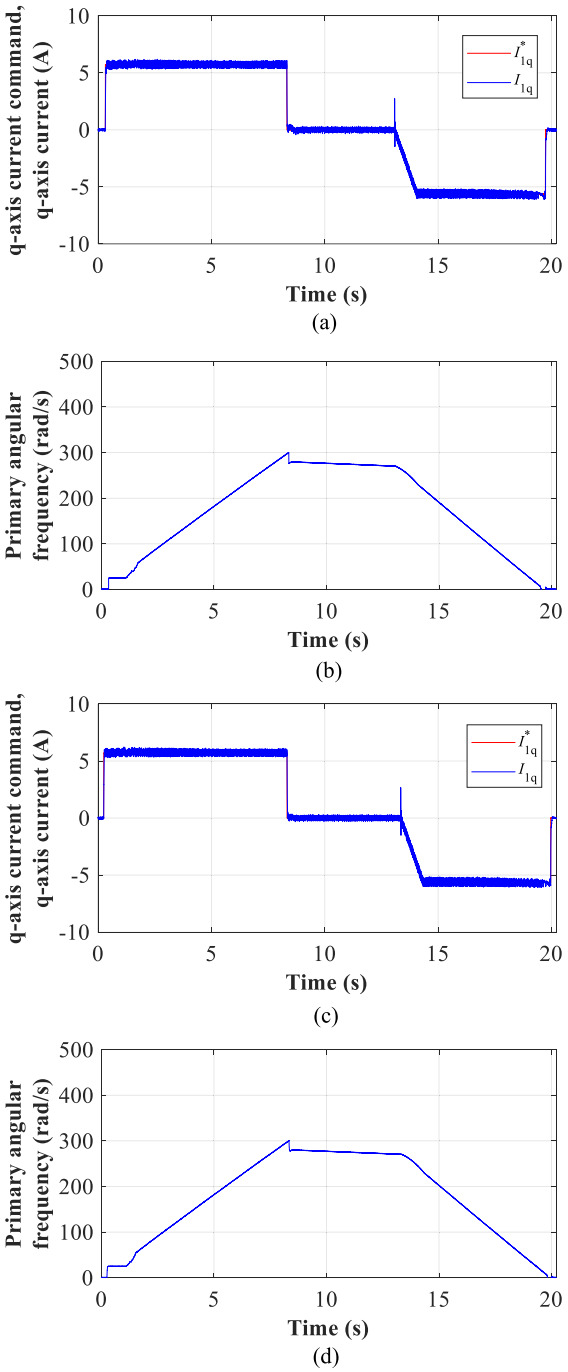

FIGURE 14. Acceleration and deceleration operation. (a) I_{1q} in the conventional IFOC. (b) ω_1 in the conventional IFOC. (c) I_{1q} in the proposed IFOC. (d) ω_1 in the proposed IFOC.

C. EXPERIMENTS OF THE CONVENTIONAL AND PROPOSED IFOC FOR VERIFICATION OF ΔR_2

Fig. 18 shows the experimental waveforms of the torque-current step response when the primary angular frequency was 250 rad/s and ΔR_2 changed. Compared with the conventional IFOC, the proposed IFOC reduces the overshoot of the torque current during the transient response; the torque-current response is close to the target response.

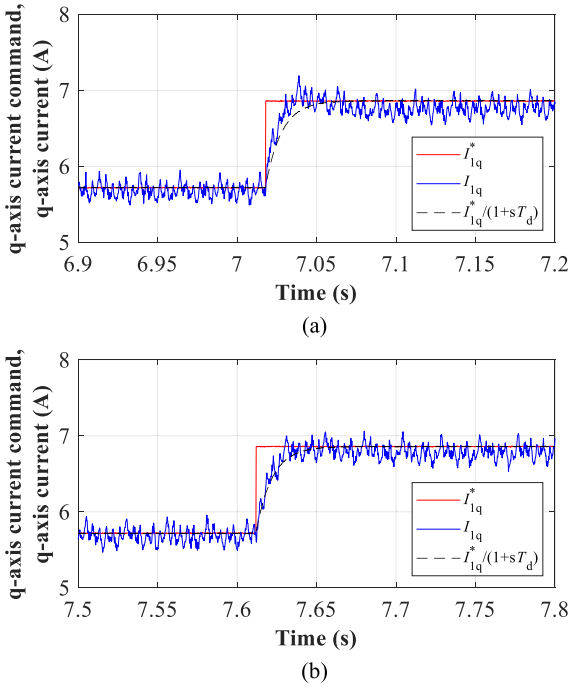

FIGURE 15. Step response in the conventional and proposed IFOC ($\omega_{10} = 250$ rad/s). (a) I_{1q} in the conventional IFOC. (b) I_{1q} in the proposed IFOC.

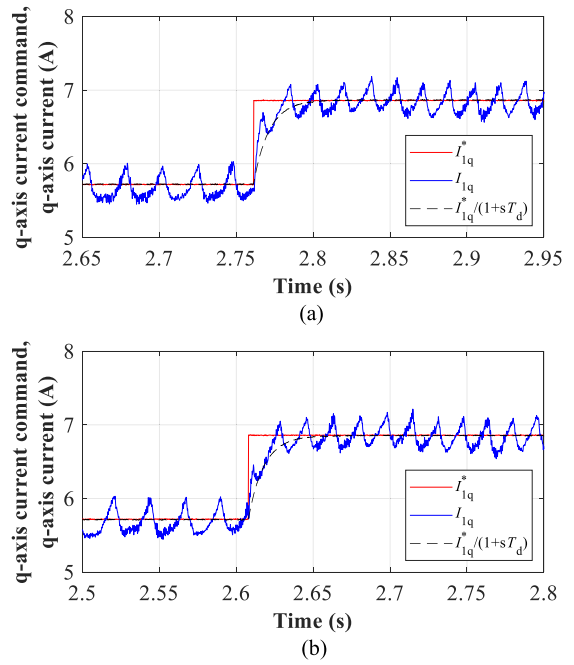

FIGURE 16. Step response in the conventional and proposed IFOC ($\omega_{10} = 50$ rad/s). (a) I_{1q} in the conventional IFOC. (b) I_{1q} in the proposed IFOC.

D. VERIFICATION OF THE CONVENTIONAL AND PROPOSED IFOC IN A WIDE SPEED RANGE

The torque-current step response of the conventional and proposed IFOC systems was verified in the primary angular frequency range of 50–300 rad/s. In the verification, the tracking error J_{te} and overshoot rate J_{ov} were calculated according to the definitions in Fig. 19, (41), and (42). In addition, the settling time is verified

$$J_{te} = \frac{1}{T_s}\int_{t_1}^{t_2}\left|\frac{I_{1qF}^{*} - I_{1q}}{I_{1qF}^{*}}\right| dt \tag{41}$$

$$J_{ov} = \frac{\max\left(I_{1q} - I_{1q}^{*}\right)}{\Delta I_{1q}^{*}}. \tag{42}$$

The torque-current step response of the conventional and proposed IFOC systems was verified in the primary angular frequency range of 50–300 rad/s. Filtering the current waveform affects the cutoff frequency component, especially in the low-speed region. Therefore, the actual current waveform, which includes harmonic components, was used for verification.

Fig. 20 shows the verification results. As the primary angular frequency increased, the tracking error and overshoot rate deteriorated in the conventional IFOC system because the magnitude of the transfer function tends to increase in this system. Conversely, the proposed IFOC realized the first-order-delay response of 100 rad/s over a wide speed range. The settling time in the proposed method is shorter than that of the conventional method because the proposed method removes the current vibration. Therefore, the proposed IFOC achieves high torque-current control performance over a wide speed range.

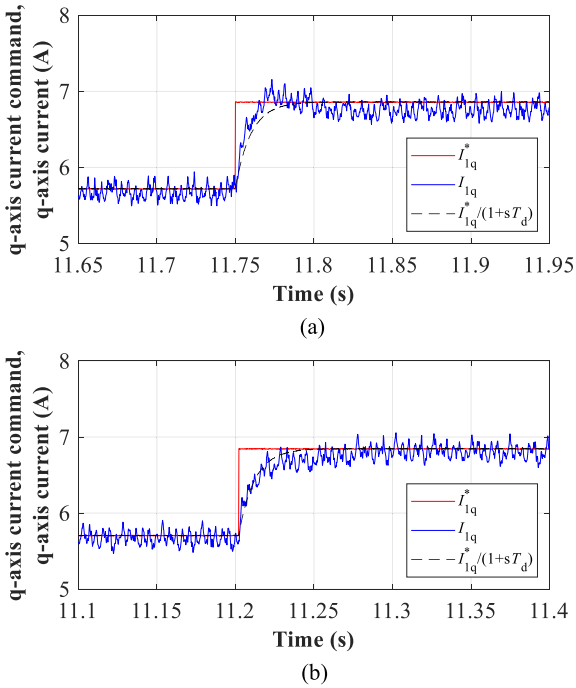

FIGURE 17. Step response in the proposed IFOC ($\omega_{10} = 250$ rad/s, $T_{ds} = 0.1T_d$, $3T_d$). (a) I_{1q} in the proposed IFOC ($T_{ds} = 0.1T_d$). (b) I_{1q} in the proposed IFOC ($T_{ds} = 3T_d$).

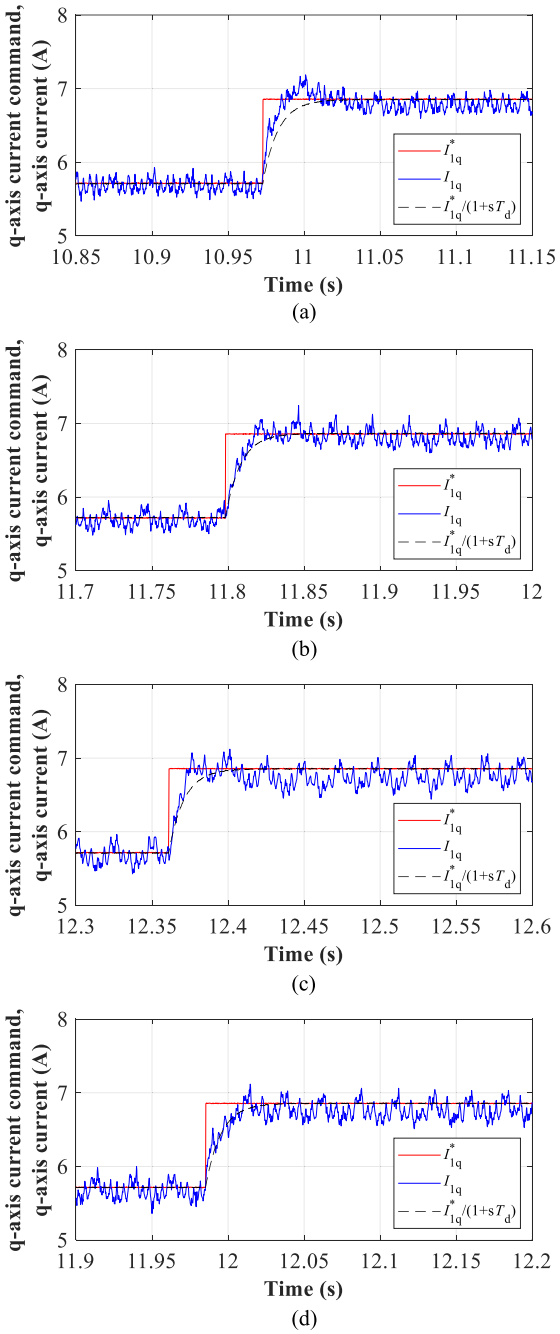

FIGURE 18. Step response in the conventional and proposed IFOC ($\omega_{10} = 250$ rad/s, $\Delta R_2 = 20,\ -10$ (%)). (a) I_{1q} in the conventional IFOC ($\Delta R_2 = 20$ (%)). (b) I_{1q} in the proposed IFOC ($\Delta R_2 = 20$ (%)). (c) I_{1q} in the conventional IFOC ($\Delta R_2 = -10$ (%)). (d) I_{1q} in the proposed IFOC ($\Delta R_2 = -10$ (%)).

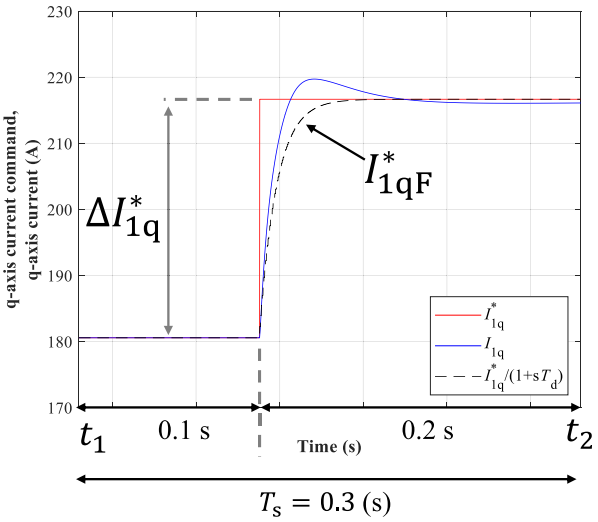

FIGURE 19. Definition in the calculation of the tracking error and overshoot rate.

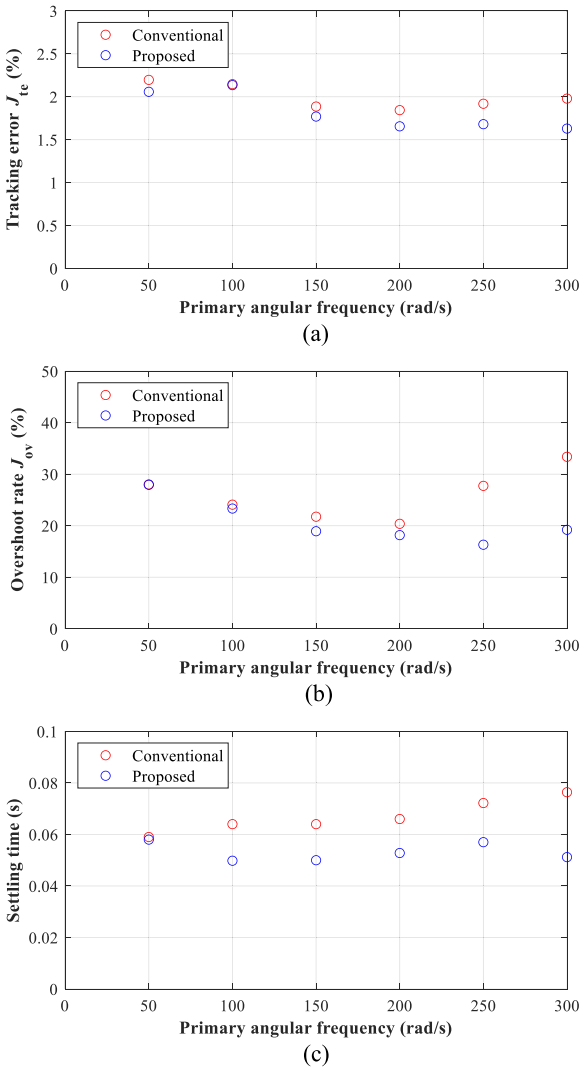

FIGURE 20. Verification of the step response of the conventional and proposed IFOC in a wide speed region. (a) Tracking error. (b) Overshoot rate. (c) Settling time.

V. ANALYSIS AND VERIFICATION OF THE CONVENTIONAL AND PROPOSED CONTROL SYSTEM WITH A 150 KW IM

A. ANALYSIS OF THE CONVENTIONAL AND PROPOSED IFOC

It is confirmed that the analytical results correspond to the simulation and experimental results in Sections III and VI. Finally, the analysis and simulation with a 150 kW IM are conducted in this section. Table 3 summarizes the IFOC of a

TABLE 3. Configuration of IM IFOC

Symbol	Quantity	Value
R_1	Primary resistance	0.0971 Ω
L_1	Primary self-inductance	30.12 mH
R_2	Secondary resistance	0.0816 Ω
L_2	Secondary self-inductance	29.93 mH
M	Mutual inductance	29.1 mH
σL_1	Primary leakage inductance in FOC	1.83 mH
T_2	Secondary time constant	367 ms
T_d	Time constant of FOC	10 ms
$I_{1\mathrm{d}}^*$	d-axis current command	93 A
$I_{1\mathrm{d}}^*$	q-axis current command	181 A

TABLE 4. Operation Point for the Analysis

Symbol	Quantity	Value
$I_{1\mathrm{d}0}$	d-axis current	93 A
$I_{1\mathrm{q}0}$	q-axis current	181 A
$\Phi_{2\mathrm{d}0}$	d-axis secondary flux	2.71 Wb
$\Phi_{2\mathrm{q}0}$	q-axis secondary flux	0 Wb
$X_{1\mathrm{d}0}$	Integral value of d-axis current deviation	0 A·s
$X_{1\mathrm{d}0}$	Integral value of q-axis current deviation	0 A·s
$I_{1\mathrm{dF}0}^*$	First-order-delay-filtered d-axis current command	93 A
$I_{1\mathrm{qF}0}^*$	First-order-delay-filtered q-axis current command	181 A
$I_{1\mathrm{dF}20}^*$	First-order-delay-filtered d-axis current command	93 A
$I_{1\mathrm{qFs}0}^*$	First-order-delay-filtered q-axis current command	181 A
$I_{1\mathrm{d}0}^*$	d-axis current command	93 A
$I_{1\mathrm{q}0}^*$	q-axis current command	181 A
$\omega_{\mathrm{s}0}^*$	Slip-angular frequency command	5.3 rad/s
ω_{10}	Primary angular frequency	– rad/s
$\omega_{\mathrm{r}0}$	Secondary angular frequency ($\omega_{\mathrm{r}0} = \omega_{10} - \omega_{\mathrm{s}0}^*$)	– rad/s

150 kW IM, which assumes a railway vehicle traction system. Table 4 lists the operational points of the analysis. The target time constant T_d of the IFOC is assumed to be 10 ms in this study.

Fig. 21 shows the closed-loop transfer function between δI_{1q}^* and δI_{1q} in the conventional and proposed IFOC systems according to (22)–(25) and (35)–(38) when the primary angular frequency is 200 rad/s. In a conventional IFOC system, the magnitude of the transfer function is large and is a second-order system. The peak magnitude is also larger than that of Fig. 2 because the inductance of a large-capacity IM is smaller than that of a small-capacity IM; and the peak magnitude of the IM plant is larger than that shown in Fig. 5, as shown in Fig. 23. Therefore, an overshoot of the q-axis current is expected in the step response. In the proposed IFOC system, the magnitude of the transfer function is –3 dB at 100 rad/s,

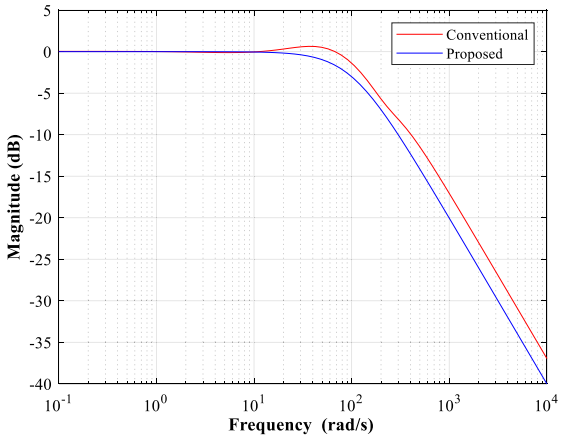

FIGURE 21. Bode plot of the closed-loop transfer function between I_{1q}^* and I_{1q} ($\omega_{10} = 200$ (rad/s)).

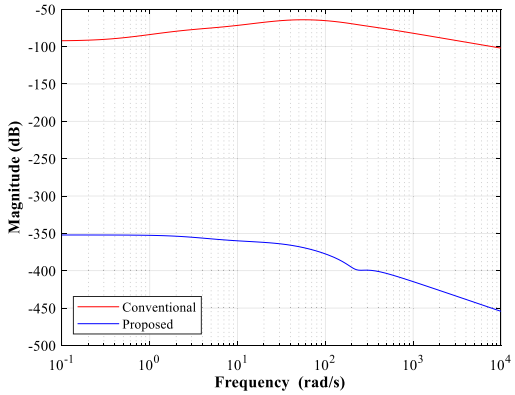

FIGURE 22. Bode plot of the closed-loop transfer function between I_{1q}^* and Φ_{2q} ($\omega_{10} = 200$ (rad/s)).

and the maximum value is 0 dB. Therefore, the proposed IFOC system is expected to be a first-order-delay system of 100 rad/s. Fig. 22 shows the closed-loop transfer function between δI_{1q}^* and $\delta\Phi_{2q}$ in the conventional and proposed IFOC systems according to (22)–(25) and (35)–(38), when the primary angular frequency is 200 rad/s. Compared with the conventional IFOC system, the proposed IFOC system reduces the q-axis secondary flux fluctuation because of the first-order-delay slip-angular-frequency control.

Fig. 23 shows the bode plots of the conventional IFOC system. The bode plots of the current controller are based on the transfer function between δI_{1q}^* and δV_{1q}^* according to (16). The bode plots of the IM plant model are based on the transfer function between δV_{1q}^* and δI_{1q} according to (21). The open-loop transfer function between δI_{1q}^* and δI_{1q} is based on (22)–(25). The peak magnitude of the IM plant causes the magnitude of the control system to be high in the high-frequency region when the primary angular frequency is high. Therefore, the magnitude of the closed-loop transfer function of the IFOC system tends to increase near the cutoff frequency when the primary angular frequency is high.

Fig. 24 shows the simulation results of the torque-current step response when the primary angular frequency was

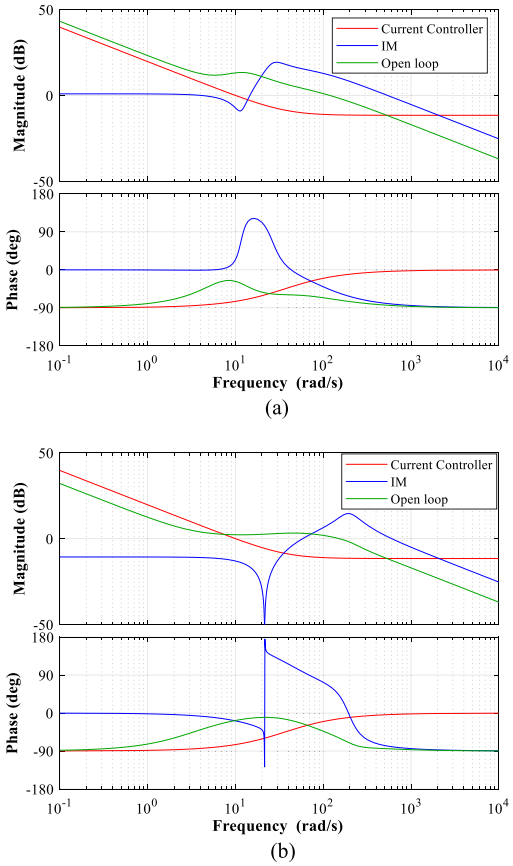

FIGURE 23. Bode plot of the transfer function of the conventional IFOC. (a) $\omega_{10} = 50$ rad/s. (b) $\omega_{10} = 200$ rad/s.

200 rad/s. In the conventional IFOC, the q-axis secondary flux fluctuates transiently when the step q-axis current command is input, and an overshoot of the q-axis current occurs owing to the coupling of the secondary flux. In the proposed IFOC, the misalignment is reduced, and the FOC and first-order-delay responses are realized.

B. VERIFICATION OF THE CONVENTIONAL AND PROPOSED IFOC IN A WIDE SPEED RANGE

The torque-current step response of the conventional and proposed IFOC systems was verified in the primary angular frequency range of 50–300 rad/s. In the verification, the tracking error J_{te} and overshoot rate J_{ov} were calculated. In addition, the settling time is verified.

Fig. 25 shows the verification results. As the primary angular frequency increased, the tracking error and overshoot rate deteriorated in the conventional IFOC system because the magnitude of the transfer function tends to increase in this system. Conversely, the proposed IFOC realized the first-order-delay response of 100 rad/s over a wide speed range. The settling time in the proposed method is shorter than that of the conventional method because the proposed method removes the current vibration. Therefore, the proposed IFOC achieves high torque-current control performance over a wide speed range.

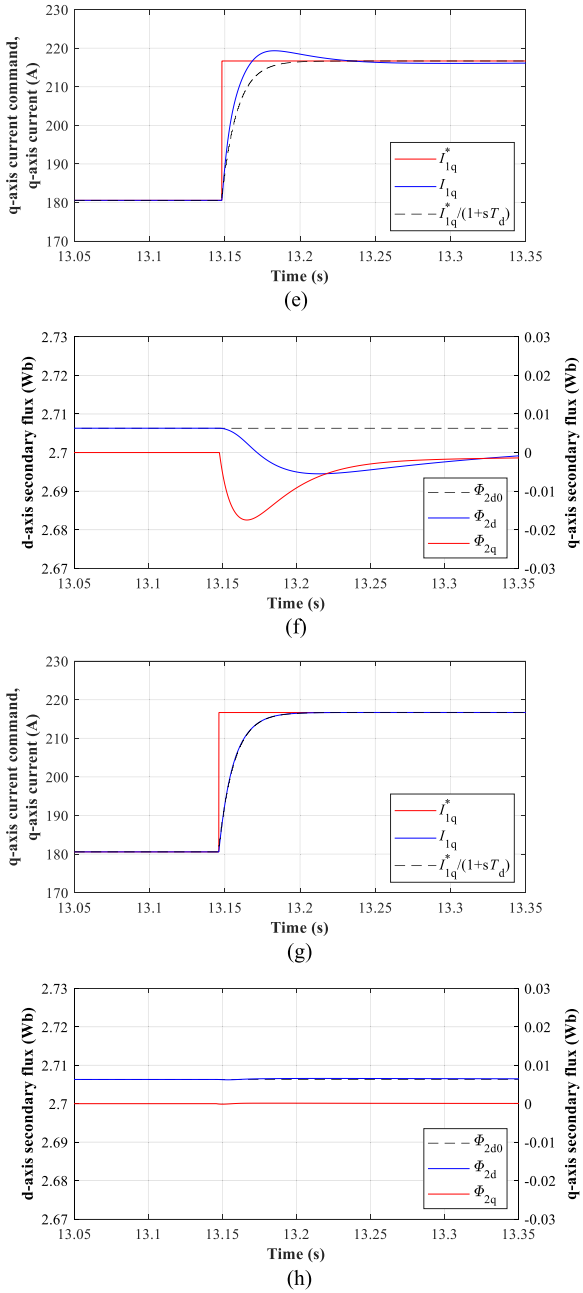

FIGURE 24. Step response in the conventional and proposed IFOC ($\omega_{10} = 200$ rad/s). (a) I_{1q} in the conventional IFOC. (b) Φ_2 in the conventional IFOC. (c) I_{1q} in the proposed IFOC. (d) Φ_2 in the proposed IFOC.

VI. CONCLUSION

An IFOC with a first-order-delay slip-angular-frequency controller, which has a simple configuration, was proposed. In the proposed method, a first-order-delay filter was added to the slip-angular-frequency controller to reduce abrupt changes in the slip-angular frequency when the q-axis current command is input. The proposed method reduces the transient fluctuation of the q-axis secondary flux and realizes sophisticated torque-current control even during a transient response.

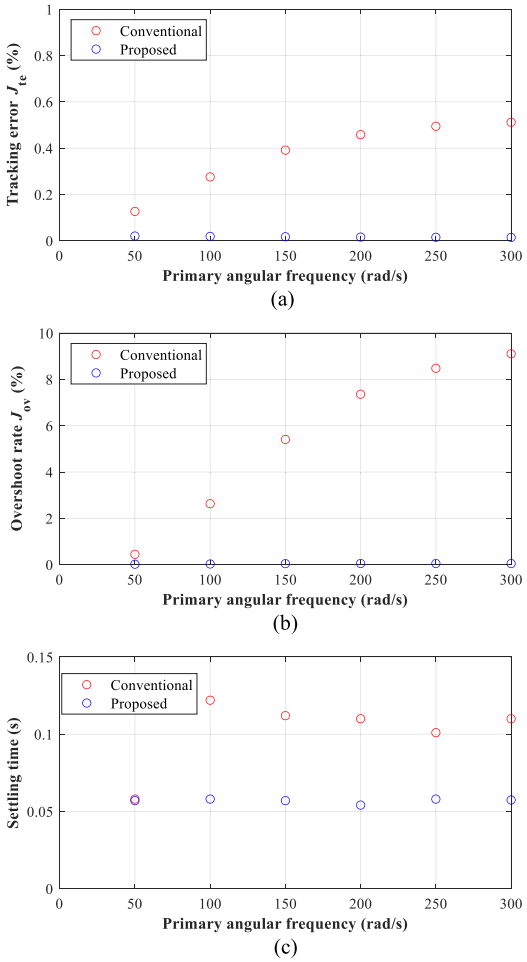

FIGURE 25. Verification of the step response of the conventional and proposed IFOC in a wide speed region. (a) Tracking error. (b) Overshoot rate. (c) Settling time.

Therefore, the proposed method makes the controller configuration simple because an additional decoupling controller is not required; and the tuning parameter is only the secondary resistance. The proposed method was verified through analysis, numerical simulation, and experiments. The proposed IFOC realizes a first-order-delay torque-current response to reduce the transient fluctuation of the secondary flux over a wide speed range; the proposed method realizes the high torque-current performance by only tuning the secondary resistance.

APPENDIX A1

Components $\boldsymbol{a_{ij}}$ of system matrix $\boldsymbol{A}_1$, except for 0, are presented as follows:

$$a_{11} = a_{22} = -\frac{R_1}{\sigma L_1} - \frac{R_1(1-\sigma)}{\sigma L_2} - \frac{K_p}{\sigma L_1}$$

$$a_{12} = -a_{21} = \omega_{10}$$

$$a_{13} = a_{24} = \frac{R_2 M}{\sigma L_1 L_2^2}$$

$$a_{14} = -a_{23} = \frac{\omega_{r0} M}{\sigma L_1 L_2}$$

$$a_{15} = a_{26} = \frac{K_i}{\sigma L_1}$$

$$a_{17} = a_{28} = \frac{R_{1s}}{\sigma L_1}$$

$$a_{18} = -a_{27} = -\frac{\omega_{10}(\sigma L_1)_s}{\sigma L_1}$$

$$a_{19} = \frac{R_{2s} I_{1q0}^*}{L_{2s} {I_{1dF20}^*}^2} \left(\frac{(\sigma L_1)_s I_{1qF0}^*}{\sigma L_1} - I_{1q0} \right)$$

$$a_{29} = \frac{1}{\sigma L_1} \times \left\{ \frac{\omega_{10} M_s^2}{L_{2s}} - \frac{R_{2s} I_{1q0}^*}{L_{2s} {I_{1dF20}^*}^2} \times \left((\sigma L_1)_s I_{1dF0}^* - \sigma L_1 I_{1d0} + \frac{M_s^2 I_{1dF20}^*}{L_{2s}} \right) \right\}$$

$$a_{31} = a_{42} = \frac{R_2 M}{L_2}$$

$$a_{33} = a_{44} = -\frac{R_2}{L_2}$$

$$a_{34} = -a_{43} = \omega_{s0}^*$$

$$a_{39} = -\frac{R_{2s} I_{1q0}^* \Phi_{2q0}}{L_{2s} {I_{1dF20}^*}^2}$$

$$a_{49} = \frac{R_{2s} I_{1q0}^* \Phi_{2d0}}{L_{2s} {I_{1dF20}^*}^2}$$

$$a_{51} = a_{62} = -1$$

$$a_{77} = a_{88} = -\frac{1}{T_d}$$

$$a_{99} = -\frac{1}{T_2}.$$

Components b_{ij} of input matrix B_1, except for 0, are presented as follows:

$$b_{11} = \frac{K_p}{\sigma L_1}$$

$$b_{12} = \frac{R_{2s}}{L_{2s} I_{1dF20}^*} \left(I_{1q0} - \frac{(\sigma L_1)_s I_{1qF0}^*}{\sigma L_1} \right)$$

$$b_{22} = \frac{K_p}{\sigma L_1} - \frac{R_{2s} I_{1d0}}{L_{2s} I_{1dF20}^*} + \frac{R_{2s}}{\sigma L_1 L_{2s} I_{1dF20}^*} \times \left((\sigma L_1)_s I_{1dF0}^* + \frac{M_s^2}{L_{2s}} I_{1dF20}^* \right)$$

$$b_{32} = \frac{R_{2s} \Phi_{2q0}}{L_{2s} I_{1dF20}^*}$$

$$b_{42} = -\frac{R_{2s}\Phi_{2d0}}{L_{2s}I^*_{1dF20}}$$
$$b_{51} = b_{62} = 1$$
$$b_{71} = b_{82} = \frac{1}{T_d}$$
$$b_{91} = \frac{1}{T_2}.$$

APPENDIX A2

Components $\boldsymbol{\alpha_{ij}}$ of system matrix $\boldsymbol{A}_2$, except for 0, are presented as follows:

$$\alpha_{11} = \alpha_{22} = a_{11}$$
$$\alpha_{12} = -\alpha_{21} = a_{12}$$
$$\alpha_{13} = \alpha_{24} = a_{13}$$
$$\alpha_{14} = -\alpha_{23} = a_{13}$$
$$\alpha_{15} = \alpha_{26} = a_{15}$$
$$\alpha_{17} = \alpha_{28} = a_{17}$$
$$\alpha_{18} = -\alpha_{27} = a_{18}$$
$$\alpha_{19} = \frac{R_{2s}I^*_{1qFs0}}{L_{2s}I^*_{1dF20}}\left(\frac{(\sigma L_1)_s I^*_{1qF0}}{\sigma L_1} - I_{1q0}\right)$$
$$\alpha_{1A} = \frac{R_{2s}}{L_{2s}I^*_{1dF20}}\left(I_{1q0} - \frac{(\sigma L_1)_s I^*_{1qF0}}{\sigma L_1}\right)$$
$$\alpha_{29} = \frac{1}{\sigma L_1} \times \left\{\frac{\omega_{10}M_s^2}{L_{2s}} - \frac{R_{2s}I^*_{1qFs0}}{L_{2s}{I^*_{1dF20}}^2} \times \left((\sigma L_1)_s I^*_{1dF0} - \sigma L_1 I_{1d0} + \frac{M_s^2 I^*_{1dF20}}{L_{2s}}\right)\right\}$$
$$\alpha_{2A} = R_{2s}\left(\frac{(\sigma L_1)_s I^*_{1dF0}}{\sigma L_1 L_{2s} I^*_{1dF20}} - \frac{I_{1d0}}{L_{2s}I^*_{1dF20}} + \frac{M_s^2}{\sigma L_1 L_{2s}^2}\right)$$
$$\alpha_{31} = \alpha_{42} = a_{31}$$
$$\alpha_{33} = \alpha_{44} = a_{33}$$
$$\alpha_{34} = -\alpha_{43} = a_{34}$$
$$\alpha_{39} = -\frac{R_{2s}I^*_{1qFs0}\Phi_{2q0}}{L_{2s}{I^*_{1dF20}}^2}$$
$$\alpha_{3A} = \frac{R_{2s}\Phi_{2q0}}{L_{2s}I^*_{1dF20}}$$
$$\alpha_{49} = \frac{R_{2s}I^*_{1qFs0}\Phi_{2d0}}{L_{2s}{I^*_{1dF20}}^2}$$
$$\alpha_{4A} = -\frac{R_{2s}\Phi_{2d0}}{L_{2s}I^*_{1dF20}}$$
$$\alpha_{51} = \alpha_{62} = a_{51}$$
$$\alpha_{77} = \alpha_{88} = a_{77}$$
$$\alpha_{99} = a_{99}$$
$$\alpha_{AA} = -\frac{1}{T_{ds}}.$$

Components β_{ij} of input matrix B_2, except for 0, are presented as follows:

$$\beta_{11} = \beta_{22} = b_{11}$$
$$\beta_{51} = \beta_{62} = b_{51}$$
$$\beta_{71} = \beta_{82} = b_{71}$$
$$\beta_{91} = b_{91}$$
$$\beta_{A2} = \frac{1}{T_{ds}}.$$

REFERENCES

[1] S. M. Tripathi and R. Vaish, "Taxonomic research survey on vector controlled induction motor drives," *IET Power Electron.,* vol. 12, no. 7, pp. 1603–1615, 2019.

[2] R. Gabriel, W. Leonhard, and C. J. Nordby, "Field-oriented control of a standard AC motor using microprocessors," *IEEE Trans. Ind. Appl.*, vol. IA-16, no. 2, pp. 186–192, Mar. 1980.

[3] J. A. Santisteban and R. M. Stephan, "Vector control methods for induction machines: An overview," *IEEE Trans. Educ.*, vol. 44, no. 2, pp. 170–175, May 2001.

[4] C. Patel, R. Ramchand, K. Sivakumar, A. Das, and K. Gopakumar, "A rotor flux estimation during zero and active vector periods using current error space vector from a hysteresis controller for a sensorless vector control of IM drive," *IEEE Trans. Ind. Electron.*, vol. 58, no. 6, pp. 2334–2344, Jun. 2011.

[5] Y. Kawabata, T. Kawakami, Y. Sasakura, E. C. Ejiogu, and T. Kawabata, "New design method of decoupling control system for vector controlled induction motor," *IEEE Trans. Power Electron.*, vol. 19, no. 1, pp. 1–9, Jan. 2004.

[6] S.-D. Wee, M.-H. Shin, and D.-S. Hyun, "Stator-flux-oriented control of induction motor considering iron loss," *IEEE Trans. Ind. Electron.*, vol. 48, no. 3, pp. 602–608, Jun. 2001.

[7] R.-J. Wai and K.-M. Lin, "Robust decoupled control of direct field-oriented induction motor drive," *IEEE Trans. Ind. Electron.*, vol. 52, no. 3, pp. 837–854, Jun. 2005.

[8] M. Comanescu, L. Xu, and T. D. Batzel, "Decoupled current control of sensorless induction-motor drives by integral sliding mode," *IEEE Trans. Ind. Electron.*, vol. 55, no. 11, pp. 3836–3845, Nov. 2008.

[9] M. A. Abbasi, A. R. Husain, N. R. N. Idris, W. Anjum, H. Bassi, and M. J. H. Rawa, "Predictive flux control for induction motor drives with modified disturbance observer for improved transient response," *IEEE Access*, vol. 8, pp. 112484–112495, 2020.

[10] T. Orlowska-Kowalska and M. Dybkowski, "Stator-current-based MRAS estimator for a wide range speed-sensorless induction-motor drive," *IEEE Trans. Ind. Electron.*, vol. 57, no. 4, pp. 1296–1308, Apr. 2010.

[11] A. Raj, Y. A. Khan, and V. Verma, "Comparative evaluation of PSO, TLBO, and JAYA based adaptive PI and FOPI controllers for vector controlled induction motor drive," in *Proc. IEEE 4th Int. Conf. Comput., Power Commun. Technol. (GUCON)*, Kuala Lumpur, Malaysia, 2021, pp. 1–6.

[12] S. Chen, T. Kai, M. Tsuji, S. Hamasaki, and E. Yamada, "Improvement of dynamic characteristic for sensorless vector-controlled induction motor system with adaptive PI mechanism," in *Proc. Int. Conf. Elect. Mach. Syst.*, 2005, pp. 1877–1881.

[13] C. C. Chan, W. S. Leung, and C. W. Ng, "Adaptive decoupling control of induction motor drives," *IEEE Trans. Ind. Electron.*, vol. 37, no. 1, pp. 41–47, Feb. 1990.

[14] I. Benlaloui, S. Drid, L. Chrifi-Alaoui, and M. Ouriagli, "Implementation of a new MRAS speed sensorless vector control of induction machine," *IEEE Trans. Energy Convers.*, vol. 30, no. 2, pp. 588–595, Jun. 2015.
[15] A. Derdiyok, M. K. Guven, H. Rehman, N. Inanc, and L. Xu, "Design and implementation of a new sliding-mode observer for speed-sensorless control of induction machine," *IEEE Trans. Ind. Electron.*, vol. 49, no. 5, pp. 1177–1182, Oct. 2002.
[16] F. F. M. El-Sousy, "Adaptive dynamic sliding-mode control system using recurrent RBFN for high-performance induction motor servo drive," *IEEE Trans. Ind. Inform.*, vol. 9, no. 4, pp. 1922–1936, Nov. 2013.
[17] F.-J. Lin, R.-J. Wai, C.-H. Lin, and D.-C. Liu, "Decoupled stator-flux-oriented induction motor drive with fuzzy neural network uncertainty observer," *IEEE Trans. Ind. Electron.*, vol. 47, no. 2, pp. 356–367, Apr. 2000.
[18] X. Fu and S. Li, "A novel neural network vector control technique for induction motor drive," *IEEE Trans. Energy Convers.*, vol. 30, no. 4, pp. 1428–1437, Dec. 2015.
[19] F. M. H. Khater, F. I. Ahmed, and F. F. M. EI-Sousy, "Analysis and design of indirect field orientation control for induction machine drive system," in *Proc. 38th SICE Annu. Conf. Int. Session Papers*, 1999, pp. 901–908.
[20] J. R. Dominguez, I. Duenas, and S. Ortega-Cisneros, "Discrete-time modeling and control based on field orientation for induction motors," *IEEE Trans. Power Electron.*, vol. 35, no. 8, pp. 8779–8793, Aug. 2020.
[21] D. G. Holmes, B. P. McGrath, and S. G. Parker, "Current regulation strategies for vector-controlled induction motor drives," *IEEE Trans. Ind. Electron.*, vol. 59, no. 10, pp. 3680–3689, Oct. 2012.
[22] S. V. K. Arun, U. Subramaniam, S. Padmanaban, M. S. Bhaskar, and D. Almakhles, "Investigation for performances comparison PI, adaptive PI, fuzzy speed control induction motor for centrifugal pumping application," in *Proc. IEEE 13th Int. Conf. Compat., Power Electron. Power Eng.*, 2019, pp. 1–6.
[23] B. Bahrani, S. Kenzelmann, and A. Rufer, "Multivariable-PI-based dq current control of voltage source converters with superior axis decoupling capability," *IEEE Trans. Ind. Electron.*, vol. 58, no. 7, pp. 3016–3026, Jul. 2011.
[24] L. A. Amézquita-Brooks, J. Licéaga-Castro, E. Licéaga-Castro, and C. E. Ugalde-Loo, "Induction motor control: Multivariable analysis and effective decentralized control of stator currents for high-performance applications," *IEEE Trans. Ind. Electron.*, vol. 62, no. 11, pp. 6818–6832, Nov. 2015.
[25] L. Amezquita-Brooks, J. Liceaga-Castro, and E. Liceaga-Castro, "Speed and position controllers using indirect field-oriented control: A classical control approach," *IEEE Trans. Ind. Electron.*, vol. 61, no. 4, pp. 1928–1943, Apr. 2014.
[26] L. Harnefors and H.-P. Nee, "Model-based current control of AC machines using the internal model control method," *IEEE Trans. Ind. Appl.*, vol. 34, no. 1, pp. 133–141, Jan./Feb. 1998.
[27] J. Jung and K. Nam, "A dynamic decoupling control scheme for high-speed operation of induction motors," *IEEE Trans. Ind. Electron.*, vol. 46, no. 1, pp. 100–110, Feb. 1999.

MASAKI NAGATAKI (Graduate Student Member, IEEE) received the M.Eng. degree in electrical engineering from the Graduate School of Science and Engineering, Chiba University, Chiba, Japan, in 2020. He is currently working toward the Ph.D. degree in electrical engineering with the Graduate School of Advanced Science Engineering, Waseda University, Tokyo, Japan.

His research interests include power electronics and motor drive.

KEIICHIRO KONDO (Member, IEEE) received the B.S. and Dr. Eng. degrees in electrical engineering from the Faculty of Electrical Engineering, Waseda University, Tokyo, Japan, in 1991 and 2000, respectively.

He was with Railway Technical Research Institute as a Senior Researcher in the rolling stock control division from 1991 to 2006. From 2007 to 2018, he attended the Electrical and Electronic Engineering Course of the Graduate School of Chiba University. Since 2018, he has been with the School of Advanced Science and Engineering, Department of Electrical Engineering and Bio Science, Waseda University, as a Professor. His research interests include power electronics, ac motor drives, energy storage systems, wireless power transmission, and their application to railway vehicle traction and electric vehicles.

Prof. Kondo is a Senior Member of the Institute of Electrical Engineers of Japan.

OSAMU YAMAZAKI received the B.Eng. degree in electrical engineering from the Faculty of Electrical Engineering, Yamagata University, Yamagata, Japan, in 1993.

He has been with Toshiba Infrastructure Systems and Solutions Co., Ltd., Tokyo, Japan, since 1993.

KAZUAKI YUKI received the M.Eng. degree in electrical engineering from the Graduate School of Electrical Engineering, Keio University, Tokyo, Japan, in 1994.

He has been with Toshiba Infrastructure Systems and Solutions Co., Ltd., Tokyo, Japan, since 1994.